U.S. DEPARTMENT OF COMMERCE
NATIONAL OCEANIC AND ATMOSPHERIC ADMINISTRATION
NATIONAL WEATHER SERVICE
NATIONAL METEOROLOGICAL CENTER

OFFICE NOTE 417

IMPLEMENTATION OF PROGNOSTIC CLOUD FOR A REGIONAL SPECTRAL MODEL

Song-You Hong, Hann-Ming Henry Juang, Q. Zhao
Environmental Prediction Center

December 1997

This is an unreviewed manuscript, primarily intended for informal exchange of information among NMC staff members

Implementation of Prognostic Cloud Scheme for a Regional Spectral Model

Song-You Hong, Hann-Ming Henry Juang and Qingyun Zhao

Environmental Modeling Center, National Centers for Environmental Prediction,Washington D.C.

December 1997

(Resubmitted to Mon. Wea. Rev.)

Address for correspondence : Dr. Song-You Hong, GSC/SAIC at NCEP/EMC, Room 207,

5200 Auth Road, Camp Springs, MD 20746, USA.

E-mail : Songyou.Hong@noaa.gov

ABSTRACT

The purpose of this study is to develop a precipitation physics package for the NCEP RSM designed to improve the skill of precipitation forecasts. The package incorporates a prognostic grid-resolvable precipitation scheme and a subgrid scale precipitation parameterization scheme with a convective trigger that explicitly couples boundary layer and convective precipitation processes. In this paper, the implementation of a prognostic cloud scheme for the NCEP RSM is described. A subgrid scale precipitation parameterization scheme was described in our companion paper (Hong and Pan 1998).

Dynamical processes such as advection and diffusion processes for liquid species are included. Eleven experiments are conducted with a grid spacing of approximately 25 km for a heavy rain case over United States during 15-17 May 1995. Special attention is given to the set-up of the prognostic grid-resolvable precipitation scheme on a spectral grid as well as the importance of dynamical processes on a mesoscale grid together with radiation feedback. Different prognostic cloud schemes, classified according to the number of predicted liquid species, are also compared.

1. Introduction

Since Zhang et al.(1989) successfully reproduced the mesoscale structure and evolution of a June 10-11 squall line case using a three-dimensional model with a standard rawinsonde data set, it has been recognized that inclusion of proper precipitation physics in a mesoscale model can lead to a significant improvement in the precipitation forecast. They argued that separate treatment of the convective portion with a cumulus parameterization scheme and the grid-resolvable portion with a prognostic cloud and precipitate scheme is the best approach for a mesoscale model. As greater computer resources have become available, prognostic cloud schemes for grid-resolvable precipitation have been incorporated into operational mesoscale models. For example, Belair et al.(1994) implemented a prognostic cloud and precipitate scheme into the Canadian regional finite-element model and successfully reproduced the mesoscale convective system studied by Zhang et al.(1989). Rogers et al.(1996) showed that inclusion in the National Centers for Environmental Prediction (NCEP) Eta model (Black 1994) of a prognostic cloud scheme with diagnostic cloud developed by Zhao and Carr (1997) led to a consistent improvement in precipitation forecasts over United States.

One of the difficulties in implementing a prognostic cloud scheme within a spectral model centers around the treatment of negative liquid species due to spectral decomposition. Some previous studies with spectral models worked around this difficulty by ignoring dynamical processes such as advection and diffusion processes for liquid species (e.g., Tiedke 1993; Mannoji 1995). However, it is obvious that the advection of cloud species is important and cannot be ignored.

This paper describes and evaluates the prognostic cloud scheme implementation for the NCEP Regional Spectral Model(RSM) designed to improve the skill of precipitation forecasts. A detailed description of the model was given by Juang and Kanamitsu (1994). Its application and subsequent development were documented in Juang et al.(1997). Descriptions of the experimental design and observations from the heavy rain case, improved convective trigger function in the cumulus parameterization scheme and its impact on the predicted precipitation are presented in our companion paper (Hong and Pan 1998). In this study we focus on the implementation of a prognostic cloud scheme within the confines of operationally available computer resources with several cloud schemes. Emphasis is placed on how each scheme affects the precipitation forecast. Eleven experiments have been conducted with a grid spacing of approximately 25 km for a heavy rainfall event over the United States during 15-17 May 1995. Section 2 describes implementation of the prognostic cloud scheme. In section 3, the experimental design for the heavy rain case is presented. The intercomparison of different cloud schemes and the sensitivity of the prognostic cloud scheme to several parameters are discussed in sections 4 and 5, respectively. A summary and concluding remarks are given in section 6.

2. Prognostic cloud scheme implementation

The cloud schemes evaluated in the RSM are classified according to the complexity of the microphysical processes (CLD#, the number of predicted water substance) included as shown in Table 1. A more complex scheme such as one including prognostic graupel, hail, and cloud number concentration is excluded from this study. Realistically, limited computer resources currently preclude the operational implementation of such sophisticated schemes. More

importantly, somewhat simpler schemes may be physically more consistent with the spatial characteristics of a mesoscale model. For example, Kuo et al.(1996) showed that in a simulation of marine cyclogenesis the graupel phase may be negligible on a mesoscale grid. In Table 1, the CLD1 scheme only includes the instantaneous removal of the supersaturation. This scheme uses the water vapor mixing ratio as its only prognostic variable. This is the current operational scheme for the Medium-Range Forecast (MRF) model (Kanamitsu 1989; Kanamitsu et al. 1991). CLD2 is the prognostic cloud scheme with ice physics developed by Zhao and Carr(1997), which is based on Sundqvist et al.(1989). In this scheme precipitate is diagnosed from the predicted clouds. The scheme was implemented into the NCEP Eta model and led to a consistent improvement in the precipitation forecast (as compared to using the diagnostic cloud scheme, CLD1) over the continental United States(Rogers et al. 1996). CLD5 follows the bulk cloud microphysics equations for cloud models developed by Lin et al.(1983), Rutledge and Hobbs(1983), and Rutledge and Hobbs(1984). The scheme introduces five prognostic moisture variables for the mixing ratios of water vapor, cloud water, cloud ice, rain, and snow. CLD3 is identical to CLD5 except that it uses a single prognostic variable for cloud/ice and another for rain/snow. Dudhia(1989) developed this formulation for computational efficiency. In the RSM, the liquid species include horizontal and vertical advections and horizontal diffusions but not vertical diffusions. On the other hand, the base fields for liquid species are set to zero when the global or larger regional domain equations do not employ the corresponding liquid species. As an example the thermodynamic equation and prognostic moisture equations are described below for CLD3.

The prognostic perturbation equations for water vapor(q_v), cloud water/ice(q_{ci}) and snow/rain(q_{rs}) species are, respectively,

$$\frac{\partial q_v'}{\partial t} = -m^2\left(u^* \frac{\partial q_v}{\partial x} + v^* \frac{\partial q_v}{\partial y}\right) - \dot{\sigma}\frac{\partial q_v}{\partial \sigma} + F_{qv}^{vdif} + F_{qv}^{hdif} + F_{qv}^{impl} + F_{qv}^{expl} - \frac{\partial q_v^{base}}{\partial t} \tag{1}$$

$$\frac{\partial q_{ci}'}{\partial t} = -m^2\left(u^* \frac{\partial q_{ci}}{\partial x} + v^* \frac{\partial q_{ci}}{\partial y}\right) - \dot{\sigma}\frac{\partial q_{ci}}{\partial \sigma} + F_{qci}^{hdif} + F_{qci}^{expl} - \frac{\partial q_{ci}^{base}}{\partial t} \tag{2}$$

$$\frac{\partial q_{rs}'}{\partial t} = -m^2\left(u^* \frac{\partial q_{rs}}{\partial x} + v^* \frac{\partial q_{rs}}{\partial y}\right) - \dot{\sigma}\frac{\partial q_{rs}}{\partial \sigma} + F_{qrs}^{hdif} + F_{qrs}^{expl} - \frac{\partial q_{rs}^{base}}{\partial t} - \frac{g}{p_s}\frac{\partial \rho q_{rs} V_t}{\partial \sigma} \tag{3}$$

The corresponding thermodynamic equation is

$$\frac{\partial T_\rho'}{\partial t} = -m^2\left(u^* \frac{\partial T_\rho}{\partial x} + v^* \frac{\partial T_\rho}{\partial y}\right) - \sigma^\kappa \dot{\sigma}\frac{\partial T_\rho \sigma^{-\kappa}}{\partial \sigma} + \kappa T_\rho\left[\frac{\partial Q}{\partial t} + m^2\left(u^* \frac{\partial Q}{\partial x} + v^* \frac{\partial Q}{\partial y}\right)\right]$$

$$+ F_T^{vdif} + F_T^{hdif} + F_T^{rad} + F_T^{impl} + F_T^{expl} - \frac{\partial T_\rho^{base}}{\partial t} \tag{4}$$

where the density temperature, T_ρ , is given by

$$T_\rho = T_v \frac{1+q_v}{1+q_v+q_{ci}+q_{rs}} \tag{5}$$

and the virtual temperature, $T_v = (1+0.608q_v)T$.

All symbols in (1-5) follow the conventional notation. The prime indicates perturbation, while the superscript *base* indicates base field values. The superscript * in variables u^* and v^* are u/m and v/m, respectively with m being the map factor. Q is $\ln(p_s)$ and $\kappa = R_d/C_p$. The F^{-}s represent tendency terms as indicated by the superscript for the variable in the subscript: *rad*(radiation), *vdif*(vertical diffusion), *hdif*(horizontal diffusion), *impl*(heating due to subgrid scale precipitation physics), and *expl*(heating due to grid-resolvable precipitation physics). The microphysical processes in the scheme contain condensation of water vapor into cloud water(ice) at water saturation, accretion of cloud by rain (ice by snow), autoconversion of cloud to rain(ice to snow), evaporation(sublimation) of rain(snow), initiation of ice crystals, and sublimation or deposition of ice crystals. The last term in (3) represents the removal of precipitates due to settling, where V_t in (3) designates the mass-weighted fall speed of the precipitates. This term is computed in grid point space following the calculation of the microphysical processes. For numerical stability, a split time-step for each model column is applied on computing the fallout terms, so that precipitate does not cross over any vertical grid within a single loop of the calculation.

Implementation of the prognostic cloud scheme necessitated several additional considerations. First, negative values of cloud water/ice crystals and snow/rain are set to zero *in grid point space (physics space)* before microphysical processes are computed. In other words, negative values in grid point space due to the vertical and horizontal advection, and horizontal diffusion calculations are eliminated. Note, however, that negative values that arise from the spectral representation are carried over during the model integration. With this treatment the negative values remain very small compared to the positive values.

Second, a split time integration approach is applied for the microphysical processes. Since the RSM employs a fairly large time step at a given grid size due to the implicit time integration scheme(e.g., physics time step, 2dt = 240s at dx = 25km), the microphysical processes could produce an unreasonable evolution of clouds even though maintaining mass conservation for all the prognostic liquid species. As indicated by Rutledge and Hobbs(1983), this probably arises due to the fact that, with a relatively large time step for microphysics calculation, relatively fast processes (such as condensation and ice nucleation) are represented as slow processes while at the same time slow processes (such as sublimation / deposition, evaporation of raindrops) become relatively fast processes. To overcome the above limitation stemming from a large time step, Fowler et al.(1996) implemented a prognostic cloud scheme into a global model, with the prescribed relaxation time that is used to express condensation / evaporation and deposition / sublimation as a finite but rapid microphysical processes. In their study, a 100 s time step was used, which is independent of the model dynamics time step. In this study, a time step of 120s is used for the calculation of all source and sink terms in microphysics.

Finally, the cloud fraction formula for radiative transfer of both long and short waves in the atmosphere is improved. In the operational version, the cloud fraction is estimated from the relative humidity RH using the method,

$$Cf = 1 - \left[\frac{1 - RH}{1 - RH_o} \right]^{0.5}, \qquad (6)$$

where RH_o is the critical value of relative humidity, which is optimized based on observations. RH_o depends upon the height of clouds. It is found that cloud fraction estimated using this method is sometimes inconsistent with the model-predicted liquid water content. For example, the cloud fraction from (6) can be high even when cloud/ice water does not exist. Furthermore, RH_o is

tuned with relative humidity based on the saturation vapor pressure with respect to water result, the formula in (6) is likely to overestimate cloud fraction in the upper troposphere. improve cloud fraction estimation, an algorithm proposed by Randall(1995) is adopted in study. This formulation utilizes both relative humidity and liquid water substance, and is g

$$Cf = RH\left[1-\exp\left(\frac{-1000q_l}{1-RH}\right)\right], \qquad ($$

where q_l means the mixing ratio for total liquid species. Since the formula in (7) effectively reduces the cloud fraction in cold clouds where cloud ice is small, it is expected to give a m reasonable radiation feedback.

All the considerations made above and the importance of various dynamical processes w examined in the sensitivity experiments presented in section 5.

3. Experimental design and case description

a. Case description

In Figs. 1 and 2, we show the surface and 500 hPa analyses at 1200 UTC 15, 16 and 17 1995, respectively. The surface maps are extracted from the daily weather maps issued by the NCEP. The 500 hPa maps are constructed from the operational Global Data Assimilation Sy (GDAS) (Kanamitsu 1989) product. At 1200 UTC 15 May 1995 (Figs. 1a, 2a) (model initialization time) a stationary front extended from Texas to the Virginia-North Carolina bord To the north of this front, a high pressure system was centered at the border between Kansas a

Missouri. At 500 hPa, a cutoff low appeared to be nearly equivalent barotropic over the west coast; little temperature advection was evident in any quadrant. There was no precipitation in Great Plains at this time. By 1200 UTC 16 May 1995(Figs. 1b, 2b), a low pressure system in mid-western Canada had crossed the US-Canada border with its center in Minnesota. As a result, a long frontal line extending from Minnesota southwestward to New Mexico had developed. Meanwhile, a surface front that was located over the south-central Unites States at 1200 UTC 15 had moved northeastward through Missouri and a frontal circulation had formed in the Great Plains. At 500 hPa, the cutoff low remained stationary and a weakening of its intensity was indicated by an increase of geopotential height at the low center. Ahead of this cutoff low a thermal ridge extended from Texas to Wisconsin. To the east of this thermal ridge, weak southwesterly flow advecting warm air to Kansas and Missouri is visible. More apparent was the warm advection at 700 hPa (not shown) in northern Texas, Oklahoma, Arkansas, Kansas, and Missouri. At this level, northwesterly flow behind the pressure trough from North Dakota to Iowa advected cold air southward. These simultaneous increases in the cold and warm advection are indicative of baroclinic energy conversion for surface cyclogenesis. In the satellite image (Fig. 3a), a cloud shield with sharp gradient ahead of the cutoff low, oriented northeastward from western Mixico to Kansas was developed. Another well developed cloud cover is centered in Missouri. During the 24hour period between 1200 UTC 15 and 1200 UTC 16 May 1995, rainfall was observed in northern Texas, along with an east-west oriented area over Kansas, Missouri, and Illinois (Fig. 4a). At 1200UTC 17 (Fig. 1c), as the surface low pressure system centered in Minnesota moved northeastward, a cold front surged southeastward extending from Texas to the Great Lakes region. A continental high pressure system with dry and cold air can be found to the

north of this front. At 500 hPa(Fig. 2c), as the cutoff low moved eastward to the Colorado-New Mexico border, the system became more baroclinic as the southwesterly wind intensified to the east of this low, and cold advection behind the pressure trough became better organized. In the satellite image (Fig. 3b), an organized cloud cover was produced in Kansas and northern Oklahoma, and another extended from Illinois to the east. Significant precipitation was found ahead of the cold front (Fig. 4b). A large area of 24-h accumulated rain greater than 32 mm covered Kansas, Missouri and Illinois. To the west of this heavy rainfall was an area of lighter precipitation over southeastern Wyoming, western Nebraska, and eastern Colorado. This rainfall seemed to be associated with upslope flow along the eastern Rockies embedded in the north-south oriented surface front.

The rainfall in Kansas, Missouri and Illinois was located in the same area for two consecutive days. This persistent rainfall led to flooding in this region. Reflecting the absence of baroclinicity at 500 hPa by 1200 UTC 16 May 1995, rainfall in that region seems to be associated with the surface warm front propagating northeastward from 1200 UTC 15 to 1200 UTC 16 May 1995 (Figs. 1a and b). It is most likely that the precipitation in the Great Plains during this period is not directly associated with baroclinic processes in the upper troposphere but is formed by frontal cyclogenesis confined in the lower tropospheric level. The upper air analyses (not shown) revealed the barotropic structure associated with the cut-off low in southern California continued until 1200 UTC 16 May 1995. After 1200 UTC 16 May 1995, precipitation in Kansas, Missouri, and Illinois formed ahead of the cold front advancing southeastward. This cold front intensified as the cut-off low finally moved eastward. Thus, rainfall during this second 24-h period seemed to be highly associated with baroclinic processes in the upper troposphere. The frontal system slowly

traveled eastward after 1200 UTC 17 May 1995 with heavy rainfall accompanying it in eastern United Sates, centered in Illinois and Indiana regions.

b. Experimental design

The model set up is identical with that discussed in Hong and Pan (1998). A more detailed description of the model and experimental design is available in their paper. The horizontal resolution is approximately 25 km over United States while in the vertical there are 28 layers in the sigma coordinate system. The model is integrated for 48 hours starting from 1200 UTC 15 May 1995.

Table 1. Summary of numerical experiments

No.	Code	Number of prognostic water species	Remarks	Domain averaged rain total(grid-resolvable), mm/48hours	Precipitatior skill score (E
	OBS			2.82	
1	CLD1	1	Diagnostic cloud	6.94 (4.14)	0.125
2	CLD2	2	Prognostic q_{ci}	5.55 (2.47)	0.162
3	CLD3	3	Prognostic q_{ci} &q_{rs}	6.00 (2.52)	0.183
4	CLD5	5	Mixed phase clouds	6.08 (2.65)	0.187
5	NGTQ	3	Negative q_{ci}, q_{rs} at grid space	4.87 (1.73)	0.181
6	DELT	3	Doubled time step for microphysics	7.00 (3.17)	0.161
7	VDCI	3	Vertical diffusion of q_{ci} considered	7.07 (3.02)	0.172
8	NOWL	3	No consideration of water loading	6.26 (2.80)	0.193
9	NORA	3	No q_{ci} information on cloud fraction	7.21 (3.33)	0.154
10	NOHD	3	No horizontal diffusion of q_{ci} & q_{rs}	6.94 (3.21)	0.189
11	NOAD	3	No advection of q_{ci}& q_{rs}	6.63 (3.47)	0.115

Table 1 provides an overview of the eleven experiments conducted. Since previous studies have examined the role of each microphysical process in the cloud physics (e.g. Zhang et al. 1988; Dudhia 1989), we do not focus on the sensitivity of individual microphysical process to the development of precipitating cloud. Rather, we emphasize the dynamical processes and the implementation issues considered in section 2. An updated subgrid scale parameterized precipitation physics from Hong and Pan (1998) is employed for all experiments. The scheme incorporates a trigger in the convective parameterization scheme that explicitly couples boundary layer and convective precipitation processes. CLD1, CLD2, CLD3 and CLD5 experiments are designed to intercompare different schemes for grid-resolvable precipitation physics and to clarify the characteristics of each scheme: CLD1-diagnostic cloud scheme, CLD2-prognostic cloud/ice water scheme, CLD3-prognostic cloud/ice and snow/rain water scheme without and CLD5-with supercooled water phase. To isolate the impact of the neglect of mixed phase in CLD3, the parameters to control cloud and precipitation processes in both CLD3 and CLD5 are set as the same as in Dudhia(1989). Since the CLD3 experiment yields the best performance, this experiment is regarded as the control run. This experiment is named the TR3M in Hong and Pan (1998). Comparisons of the CLD1, CLD2, CLD3 and CLD5 schemes will be presented in section 4. The remaining experiments in Table 1 are sensitivity tests used to examine the impact of dynamical processes and evaluate the previously mentioned implementation issues in the prognostic cloud scheme, which will be presented in section 5. Note that each run is conducted by changing an option in the CLD3 experiment.

The NGTQ experiment which allows negative values for cloud species in grid point space is used to explore the impact of the negative values on the modeled cloud evolution. In the calculation of microphysical processes, the changes are calculated by setting the negative value for liquid species as a very small positive value to avoid a floating point exception. Thus, this experiment carries the negative value generated from the dynamical processes including diffusion and advection processes. The DELT experiment uses the same time interval for microphysical processes as is used for other physical processes (= 240s for this study). In the CLD3 experiment two minor loops are iterated with a 120s time step. Thus, The DELT experiment provides assessment for the split time step for microphysical processes. The VDCI experiment includes vertical diffusion of cloud species to evaluate the importance of this process. The NOWL experiment replaces T_p by T_v in (5) to examine the importance of the water loading effect of liquid species. The NORA experiment employs the operational cloud fraction formula that was discussed in (6), and serves to investigate the importance of the radiation feedback by the predicted precipitation. The NOHD and NOAD experiment are designed to investigate the importance of horizontal diffusion, and vertical and horizontal advections of cloud species, respectively.

Also shown in Table 1 is the 48-h accumulated domain averaged rain. The value in the parenthesis represents the grid-resolvable rain contribution to the total rain. The equivalent threat scores(ETS) of the precipitation forecast are presented to compare the skill of precipitation forecasts. Whereas the simple threat score is the quotient of the intersection of the observed and forecast areas of precipitation divided by the union of these areas, the ETS refines the definition by accounting for apparent skill derived only from random chance (Rogers et al. 1996). The scores are computed over the United States using forecast precipitation and observed precipitation

computed by averaging rain gage data within each model grid cell. Scores are averaged in precipitation categories for the two day forecast period. Together with domain averaged total precipitation amount, the ETS gives a measure of the skill of precipitation forecasts. Values in the table are the average over all precipitation categories. Although the ETS in each precipitation category is robust in representing the precipitation skill, the average seems to be sufficient to compare the skill of precipitation predictions from each experiment for a single case study. It is important to note that at NCEP the ETS and bias scores are routinely computed at 80 km grid. Both model forecasts and observation are interpolated to that grid. Hence, higher precipitation bias from the model results than the observation is not only due to the model's error but also due to no observation station every 25 km over United States. This results in the reduction of the ETS than when it is computed on 80 km grid. Therefore, comparison of the scores in Table 1 is worthwhile, but not for magnitude. Nevertheless, the CLD3 experiment showed a bias of 1.2 when it was computed on 80 km grid, indicating high precipitation biases for all experiments except for the NGTQ experiment.

4. Intercomparison of grid-resolvable precipitation physics schemes

In this section, we compare the CLD1, CLD2, CLD3 and CLD5 experiments. Since the CLD3 and CLD5 results are very similar in many respects, discussion of CLD5 results will be skipped, except when needed.

Figure 5 shows the predicted 24-h accumulated precipitation valid at 1200 UTC 16 May and at 1200 UTC 17 May 1995 as forecasted in the CLD1, CLD2, and CLD3 experiments. It is apparent that the grid-resolvable rain distribution noticeably differs between the simulations. The distribution of subgrid scale rain also varies from one to another, but not as much as the grid-

resolvable rain. In the 24-h forecast(Figs. 5a, 5c, and 5e), the CLD1 and CLD2 experiments produce isolated areas of resolvable rain. Maximum values in Kansas region from the CLD1 and CLD2 experiments are as high as 170 mm, and 70 mm, respectively. On the other hand, the CLD3 experiment does not produce such isolated grid-resolvable rain. Of course, we realize that the observed precipitation cannot be partitioned into subgrid scale and grid-resolvable portion and so the partitioning of precipitation into subgrid and grid-resolvable cannot be confirmed. However, based on the precipitation forecast skill and precipitation pattern the amount of grid-resolvable rain produced by the CLD1 and CLD2 experiments can be regarded as excessive. The excessive rainfall from the CLD1 experiment is due to the positive feedback between latent heating and mesoscale motion which occurs when liquid species are diagnosed without a memory as a prognostic variable. This feedback mechanism was suggested by Zhang et al. (1988). The excessive grid-resolvable rain in the CLD2 experiment seems to be due to the absence of the precipitate loading effect in the scheme. In the 48-h forecast the CLD1 experiment reveals isolated contours of grid-resolvable rain over Colorado while the CLD2 and CLD3 experiments produced a more realistic distribution of grid-resolvable rain over this area. Over the heavy precipitation area in Missouri and Illinois, the CLD2 experiment with the diagnosed precipitate produces more widespread subgrid scale and grid-resolvable rain than do the CLD1 and CLD3 experiments. The reduction of sub-grid scale precipitation over Oklahoma in the CLD2 experiment also noticeably differs from the other two experiments. Although the reason to cause such a different precipitation distribution in the CLD2 experiment from the results from other experiments is unclear, it may be due to the characteristic of microphysical processes and associated large-scale feedback mechanism, which will be described below.

In Fig. 6, the domain averaged precipitation amounts of total, subgrid scale, grid-resolvable rain, and the ratio of subgrid scale rain over total rain derived from the CLD1, CLD2, CLD3 and CLD5 experiments are compared. It is evident that the diagnostic cloud scheme(CLD1) produces more grid-resolvable rain and less subgrid scale rain than when cloud species are treated as prognostic variables. The subgrid scale rain has a similar time trend for all the experiments while the grid-resolvable rain differs. It is interesting to note that grid-resolvable rain with the prognostic cloud scheme (CLD2) increases steadily with time while others do not. The reduction of grid-resolvable rain amounts with the prognostic cloud schemes during the 12-h forecast time is likely due to the finite residence time of liquid species before reaching the ground by falling velocity through various microphysical processes. To clarify the difference in the microphysics between the two schemes, the volume averaged q_{ci} in entire model grid is computed and shown in Fig. 7. It is clear that the prognostic cloud water/ice scheme with diagnosed precipitate(CLD2) reveals higher amounts of q_{ci} than the scheme with prognostic precipitate(CLD3, CLD5). The ratio is as high as 3:1 at the 30-h forecast, indicating that the net amount, source minus sink, of cloud species is greater in the CLD2 scheme than in the CLD3 scheme. It is difficult to clarify the reason why this difference appears, because microphysical processes in the CLD2 scheme are represented in a different way from the CLD3 and CLD5 schemes. A lower saturation threshold than 100 % in the CLD2 scheme (85 % in this study) may be one of the reasons.

In Fig. 8, it can be seen that the CLD1 experiment produces a more destabilized troposphere than the CLD3 experiment. A moisture deficit is distinct within the entire troposphere with the increase downward. Realizing that the amount of total precipitation is higher than that from the CLD3 experiment, the warmer temperature in the lower troposphere and colder temperature in the

upper troposphere indicate the existence of an unphysical feedback between low-level convergence, diabatic heating, and upward motion which is due to the lack of stabilized processes such as evaporation, melting, and water loading effects. Although the moisture deficit is most distinct in the lowest 200 hPa, the CLD2 experiment does not reveal a systematic temperature bias as compared to the CLD3 experiment. This less distinct systematic departure is not only due to diagnosed precipitate treatment in the CLD2 scheme, but also, is due to the different control parameters in microphysical processes between the two schemes. Overall, the temperature and moisture from the CLD5 experiment shows a little deviation from those in the CLD3 experiment. Temperature is slightly higher above 600 hPa and lower below, indicating a stronger stabilization in the CLD5 experiment. Many processes may be responsible for these differences since the interaction between the thermodynamic and dynamical processes is nonlinear. We come to the above conclusions based primarily on the differences in the microphysical processes between the CLD3 and CLD5 schemes. A primary difference between the two schemes is that in the CLD5 experiment melting and freezing processes occur within a deeper layer while they occur as instantaneous processes at the freezing level in the CLD3 experiment. Therefore, more heating above (more cooling below) 600 hPa would more likely occur due to more freezing (more melting) by the CLD5 scheme. The melting difference might be expected to increase downwards because when all the melting occurs just at the freezing level, as in the CLD3 experiment there may be subsidence causing the cooling to spread down a little but its effect is limited by the stability. With the CLD5 scheme the snow can melt even below where the subsidence reaches in the CLD3 scheme so the cooling is deeper. Nevertheless, the overall impact of this mixed phase to the large-scale feedback is not significant.

From the results we examined, the bulls-eye problem which appears in the diagnostic cloud physics experiment(CLD1) was clearly removed by employing the sophisticated grid-resolvable precipitation physics. However, it is important to note, as discussed in Hong and Pan (1998), that the convection scheme with the operational trigger did not remove the localized grid-scale rain in Kansas during the 24-h forecast period. Furthermore it distributed the grid-scale rain from Indiana eastward, too far northeast. This was true even in the case of prognostic cloud and precipitate employed for the grid-resolvable precipitation physics, as in the CLD3 experiment. They demonstrated that the same convection scheme with different grid-resolvable physics shows very similar axes for the grid-resolvable rain in Indiana eastward, and that the new trigger in the convection scheme has the axis notably to the south. In other words, the experiments differ only in the convection trigger, sharing the same grid-resolvable schemes, yet they differ in the mentioned area in the locus of the grid-resolvable maxima. The results in this study reinforce the fact that the same convection scheme with different grid-resolvable precipitation physics shows a very similar axis for the grid-resolvable rain in that area (Fig. 5b, 5d, and 5f). The significant impact on the grid-scale precipitation due to parameterized convection was addressed by Kuo et al.(1996).

As mentioned earlier, the differences between the CLD3 and CLD5 experiments are not significant except for a slight increase in the grid-resolvable rain in CLD5 (Fig. 6, Table 1). This suggests that the mixed phase in the microphysics is of negligible significance for the predicted precipitation in this case. This is in line with the theoretical basis of the scheme in the CLD3 experiment as Dudhia (1989) formulated it. As a result, it is concluded that the prognostic cloud and precipitate scheme with ice physics (CLD3) may be adequate for the grid-resolvable precipitation physics in a operational mesoscale model.

5. Sensitivity experiments

In Table 1, the ETSs from the sensitivity experiments are comparable or worse compared to that from the CLD3 experiment. Recall that each experiment changes one option from the CLD3 experiment listed in Table 1. Since all experiments, except the NGTQ experiment, increase precipitation amounts, bias scores are worse than the CLD3 experiment. The CLD3 experiment produced more precipitation than observed by a factor of 2.1 in a domain averaged sense (Table 1). Considering the two skill scores mentioned above, it is judged that all sensitivity experiments showed comparable or worse skill scores in the precipitation forecasts. In particular, the impact of advection for clouds and precipitates (NOAD) is very significant.

Figure 9 shows the height-time crosssections of q_{ci} and q_{rs}, vertical motion, and relative humidity from the CLD3 and NTGQ experiments. From the comparison of Figs. 9a and 9b, it can be seen that the CLD3 experiment shows a realistic distribution of q_{ci} and q_{rs} in association with the stratiform cloud in the upper troposphere and the precipitate below. Compared to the CLD3 experiment, the NGTQ experiment reveals a shallow stratiform cloud layer with negative values of q_{ci} beneath. These negative values are of the same order as the nearby positive values. The reduction of cloud species to negative values may be related to the vertical advection processes, as shown in Figs. 9c and 9d. The negative values of q_{ci} from the NGTQ experiment appear where vertical motions are strong. The distribution of q_{rs} is highly localized in horizontal grid space (not shown). Thus, its negative value seems mostly to be due to the horizontal advection. In turn, negative values of q_{ci} and q_{rs} act as a sink of water vapor. In such situations clouds could not be generated even when the air column is supersaturated until the values become positive. This

misleading feature in the microphysical processes produces an unrealistic feedback to the larger-scale dynamic circulation. The interaction between the dynamic and thermodynamic processes is not straightforward. Despite this, it can be seen that the resulting modeled atmosphere from the NGTQ experiment has a weaker vertical motions with smaller horizontal and vertical scales than does the CLD3 experiment. Relative humidity in the upper troposphere is also smaller. Comparison of domain-averaged thermodynamic profiles (not shown), indicates that the NGTQ experiment produced a more stabilized atmosphere than the CLD3 experiment, in conjunction with the less intense dynamic circulation. This results in the misleading improvement in the skill of precipitation bias (see the last paragraph of section 3).

In Fig. 10, the 24-h accumulated precipitation at the 48-h forecast time valid at 1200 UTC 17 from the DELT experiment is shown. It is obvious that the grid-resolvable rainfall is widespread compared to that from the CLD3 experiment (Fig. 5f). The distribution of grid-scale precipitation over the Ohio valley is much farther northward than seen in the CLD3 run. A difference is also discernible in the distribution of subgrid-scale rain. For example, the DELT experiment produced much less subgrid-scale and grid-scale rainfall in Kentucky. To clarify the difference between the two experiments, the comparison of q_{ci} and q_{rs}, and the difference of relative humidity at the point A, marked in Fig. 10, are shown in Fig. 11. At this point, both experiments produced comparable amounts of grid-scale and subgrid-scale rain (not shown). A peak intensity of grid-scale rain appeared at 1900 UTC 16 in both expriments. Compared to the CLD3 experiment, the DELT experiment shows an early onset of grid-scale rain that accompanies the low level cloud below 700 hPa (Figs. 11a and 11b). With time, q_{ci} and q_{rs} tend to be higher in the DELT experiment that those from the CLD3 experiment. Unreasonably large values of q_{ci} and

q_{rs} appear in the DELT experiment in the middle to upper atmosphere when grid-scale rain activity is mature. In the DELT experiment, maximum values of q_{ci} and q_{rs} are as high as 3.8 gkg^{-1} and 12 gkg^{-1}, respectively, at 400 hPa at 1900 UTC 16, while in the CLD3 experiment q_{rs} has a maximum of 5 gkg^{-1} at that level, and q_{ci} ranges below 0.7 gkg^{-1} in the stratiform cloud region. We have noticed that this unrealistically localized q_{ci} and q_{rs} distribution in the middle to upper troposphere is a common feature in the DELT experiment. This may stem from the fact that, in the DELT experiment with a 240 s time step, relatively slower microphysical processes such as evaporation and sublimation become faster while relatively faster processes such as condensation and ice nucleation become slower compared to those in the CLD3. This behavior compromises the microphysics underlying these processes. For example, the early onset of low level cloud below 700 hPa and associated precipitation formation in the DELT experiment are found to be due to supersaturation in that layer (Fig. 11c). Higher relative humidities are distinct where low level cloud is produced in the DELT experiment. Because condensation with a 240s time step cannot remove supersaturation as efficiently as in the case of a 120s time step, rain water forms by autoconvection in the DELT experiment, while cloud water evaporates in unsaturated condition in the CLD3 experiment. Note that evaporation of cloud water is an instantaneous process during a time step in the presence of subsaturation.

Cold cloud in the upper troposphere experiences the more complicated processes of ice phase physics than in warm cloud. The CLD3 experiment showed a nearly saturated profile during the mature stage of the grid-scale rain activity during 1800-2000 UTC 16 (not shown). However, a numerical instability-like evolution of relative humidity is apparent in the DELT experiment. As mentioned earlier, with a large time step the ice nucleation process would not be as efficient in

removing the supersaturation as in nature. Furthemore, the amount of adjustment due to some microphysical processes would bound to a limit of water substance that remains in the atmosphere. From a single column test, with a large time step, the depositional growth of ice crystal could be as high as the amount of supersaturated water vapor irrespective of the property of existing ice, leading to a quick drop of relative humidity. At next time step, a totally different microphysical process, sublimation, resulted in a saturated layer. In other words, one process is dominant at one time and another is dominant at the following time step, while with a small time step all microphysical processes occur simultaneously. These less physically based adjustments cause the unrealistic evolution of liquid species. In contrast, a further decrease in the time step below 120 s does not significantly affect the results.

In Fig. 12, the vertical profiles of θ_e and θ_{es} from the CLD3 and VDCI experiments are compared. The VDCI experimental results are colder and more moist below the 780 hPa level, and warmer and drier than the CLD3 results above it. Note that boundary layer vertical mixing of q_{ci} does not change the θ_e distribution. We explain this behavior as follows : As supersaturation produces a low-level cloud within the PBL, a nonlocal large eddy transports the q_{ci} efficiently within the mixed layer. The transported q_{ci} immediately evaporates when the level is subsaturated, which results in the cooling and moistening at the level. Through this process the environment becomes more favorable to initiate convection due to the increased relative humidity in subcloud layer. The enhanced grid-scale rain from the VDCI experiment seems to be due to the increased detrainment of water vapor at the convective cloud top. An increase of q_{ci} was obtained in the upper troposphere from the VDCI experiment (not shown). As a result of these mechanisms the vertical diffusion seems to increase not only the subgrid scale and but also grid-resolvable rain

(Table 1). Meanwhile, vertical diffusion of cloud species were omitted in this study to achieve a better precipitation forecast skill. However, we speculate that this process may need to be incorporated to simulate the cloud evolution in a more realistic fashion unless a high precipitation bias appears in the model.

In Fig. 13, the difference of domain averaged short and long wave radiative heating in the NORA and CLD3 experiments is presented. In terms of the ETS and domain accumulated precipitation (Table 1), the impact of different cloud fraction formulation between the two experiments is significant. The ETS from the NORA run is as low as in the case of the DELT experiment. The differences for both short wave and long wave radiative heatings are most significant between 300 hPa and 850 hPa. The impact of the long wave portion is larger. The operational cloud fraction formula in (6) tends to overestimate the cloud fraction in cold clouds, as described in section 2. This overestimation of cloud fraction is mostly due to the operational radiation package using a relative humidity threshold, RH_o in (6), with respect to water. Given the increase of the relative humidity for the same value of water vapor when using ice physics, the cloud fraction is always overestimated in cold clouds. This high amount of cloud fraction causes a significant degradation of the skill in the precipitation forecast, through the radiation-precipitation feedback mechanism. The new formula in (7) improves the radiation feedback by effectively reducing the cloud fraction when q_{ci} is small. Nevertheless, it was found that the new cloud fraction formula still tends to overestimate cloud fraction compared to the optimized value from the operational formula without ice physics in the model. Tuning a relative humidity threshold, RH_o in (6) with respect to ice maybe another way to alleviate the problem using the operational formula. Evaluation of the threshold values is being undertaken based on the observation data sets

for radiation climatology. As a result, despite this improvement we feel that a new radiation package which directly computes the emissivity from cloud water/ice water will be needed in the future.

Figure 14 shows the difference of time-area averaged temperatures between the NOWL and CLD3 experiments for the 48-h forecast period. Below 600 hPa the NOWL experiment has lower temperatures compared to the CLD3 experiment, indicating a stronger stabilization in the NOWL experiment. The lower troposphere might be cooler when water loading is neglected because upward motion would be more likely occur. This behavior is consistent with the previous studies(e.g. Zhang et al. 1988), in a sense that water loading plays a role in stabilizing the atmosphere when liquid species exist. Zhang et al. (1988) highlighted that the hydrostatic water loading effect is an important effect among the microphysical processes, together with evaporation of rain drops and melting of snow, in suppressing the development of excessive grid-scale rain. In contrast, the overall impact of water loading on the precipitation is not significant in this study. For example, the difference of temperature ranges below 0.1 K below 600 hPa. The moisture deviation was also negligible (not shown). The ETS and bias scores are very comparable for both experiments (Table 1). The precipitation distribution is very similar for both experiments without a discernible unrealistically localized grid-scale rain from the NOWL experiment (not shown). From the preliminary sensitivity experiments, evaporation and melting processes were found to be the major processes responsible for the reduction of localized grid-scale rain processes in this study, as pointed out Zhang et al.(1988). A possible explanation for this discrepancy is that water loading is considered in all the governing equations in the current study while Zhang et al. (1988) considered this effect only in the hydrostatic equation.

In Fig. 15, the distribution of 250 hPa q_{ci} derived from the CLD3 and NOHD experiments at 1200 UTC 16 is compared. The distribution of q_{ci} from the CLD3 experiment is generally comparable with the satellite image (Fig. 3a). Note that the comparison cannot be directly confirmed. The satellite imagery is one hour and fifteen min. prior to the valid time of the forecast. In addition, there is an uncertainty in comparing the visible satellite image and the 250 hPa q_{ci} distribution. Despite these uncertainties, it can be seen that the model was capable of capturing the major features associated with the cloud evolution. For example, a cloud shield with a sharp gradient ahead of the upper level cutoff low, oriented northeastward from western Mexico to Kansas, was very well organized. The model also predicted a cloud free area between this long cloud shield and the cloudy area located over Indiana, Illinois, northeastern Missouri and western Kentucky. In addition, a long cloud band to the north of the heavy precipitation area was well simulated.

From Figs. 15b and 15c, it can be seen that the horizontal diffusion of q_{ci} plays a positive role in q_{ci} evolution by removing widespread light values and redistributing excessive values, the overall effect being a more realistic distribution. Without horizontal diffusion of q_{ci} and q_{rs}, the model produced similar precipitation patterns but greater amounts (Table 1). The ETS score is comparable for both experiments, but the increase of grid-scale rain is noticeable in the NOHD experiment. Thus, we may say that horizontal diffusion of the liquid species has a positive impact because it removes unrealistic features.

As indicated in Table 1, advective processes for clouds and precipitates are the most significant factor in the modeled cloud or synoptic scale evolution. Fig. 16 shows the 24-h accumulated precipitation amounts from the NOAD experiment. Compared to the CLD3

experiment (Fig. 5e and 5f), it can be seen that without advection, excessive grid-resolvable rain is generated in some areas. It is interesting to note that in the 24-h forecast the axis of subgrid scale rain is located in northern Oklahoma, which is much farther to the south than in the CLD3 experiment. It is not possible to isolate the direct impact of non-advecting liquid species on the predicted precipitation and associated synoptic features. However, we speculate that the big difference in the convection forecast over heavy precipitation regions seems to have influenced the down stream location of the predicted precipitation and embedded synoptic patterns in the 48-h forecast. This behavior was found when the operational convection trigger was employed (Hong and Pan 1998). The ETS from the NOAD experiment is as bad as in the experiment with the operational convective trigger in Hong and Pan(1998). Fig. 17 compares the volume averaged q_{ci} from the CLD3 and NOAD experiments. It can be seen that the NOAD experiment reveals higher amounts of q_{ci} than the CLD3 experiment. This implies that the removal processes of cloud species are slower than the generation processes when advection is ignored, as was the case of the CLD2 experiment in Fig. 7. It is therefore concluded that advection plays an important role in generating realistic cloud evolution by transporting liquid species to a right place. The advection of liquid species cannot be neglected at mesoscale grid resolutions.

6. Summary and concluding remarks

A new precipitation physics package for the NCEP RSM designed to improve the precipitation prediction skill during the convection season over United States is proposed. The new physics package includes a prognostic cloud scheme which explicitly treats the cloud microphysical processes, and a revised convective parameterization scheme based on the concept of convective

trigger functions which explicitly couple boundary layer and convection processes. The new package has been extensively tested with a grid spacing of approximately 25 km over United States for a heavy rainfall case during 15-17 May 1995. This paper describes and evaluates the prognostic cloud scheme implementation for the NCEP RSM. Description of the convective trigger function, the heavy rain case, and the model and experimental design are presented in detail in our companion paper (Hong and Pan 1998).

In this study we focus on the implementation of a prognostic cloud scheme within the confines of operationally available computer resources with several cloud schemes. Special emphasis is placed on how each scheme influemces the precipitation forecast. The treatment of the prognostic liquid species includes the same dynamical processes as for the water vapor variable, excluding vertical diffusion. The problem of negative values in a spectral model for liquid species is addressed by setting negative values to 0 in grid point space. However, the negative values due to spectral transformation are retained in spectral space. A split time integration approach is applied for the microphysical processes. In addition, a cloud fraction formula including liquid species information is employed for realistic radiation feedback. Eleven experiments were designed to investigate the sensitivity of the precipitation forecast to the set-up of the prognostic cloud scheme and to compare several grid-resolvable precipitation schemes.

From the intercomparison among different grid-resolvable precipitation physics schemes, we found that the prognostic treatment of cloud/ice and rain/snow allows for a much more realistic simulation of the heavy precipitation case. The diagnostic precipitate scheme with prognostic cloud partially removes some excessive rainfall due to the grid-resolvable precipitation process which exists in the diagnostic cloud scheme, but surface precipitation is not as organized as with

the prognostic precipitate scheme. On the other hand, the detailed treatment of microphysical processes with supercooled water does not significantly affect the model results. It is important t note that the sophisticated grid-resolvable precipitation physics alone is found to be responsible fc the reduction of excessive grid-scale rain due to the unrealistic feedback between low-level heating, surface pressure fall, low-level moisture convergence, and upward motion, as pointed ou by Molinari and Dudeck(1986) and Zhang et al.(1988). However, Hong and Pan(1998) demonstrated such a feedback can occur due to the characteristics of the parameterzed convection even though sophisticated microphysical processes are included. The results using the convection scheme with the operational trigger did not only generate the excessive grid-scale rain, but also changed significantly the larger-scale patterns downstream.

From the sensitivity experiments regarding the implementation set up of the prognostic cloud scheme, the negative value treatment, which enforces a lower bound of 0 for clouds and precipitates in grid point space, effectively removes unrealistically large negative values of prognostic liquid species which result from the dynamical processes. As an alternative, a semi-lagrangian method in treating water substance is underdevelopment. A finer time step of 120s for microphysical processes solves the unphysical evolution of liquid species when the model employs a large time step. The vertical diffusion of q_{ci} increases the subgrid scale rain as well as grid-resolvable rain due to enhanced vertical mixing of cloud water. Including cloud information in the radiation scheme improves the cloud fraction calculation by removing cold cloud when predicted values of cloud water/ice water are small. However, it is desirable to develop a radiation scheme which directly incorporates the cloud properties. Horizontal diffusion plays a role in reproducing cloud evolution in a realistic fashion by effectively removing light spurious cloud and

redistributing unrealistically localized liquid species when it is not considered. Horizontal and vertical advection of liquid processes are essential to the realistic simulation of cloud evolution and cannot be ignored.

From the results we have examined it is concluded that the prognostic cloud scheme has been successfully implemented in a regional spectral model. It is also noted that the proper set-up of prognostic grid-resolvable rain scheme is very important and the impact of the implementation set-up (e.g. advection for liquid species) is more significant to modeled precipitation than the choice of different schemes. As stressed in Hong and Pan (1998), a proper treatment of the parameterized convection in subgrid scale precipitation physics is crucial to achieve a realistic cloud simulation in grid-resolvable precipitation scheme. Within the limitations of available computer resources, the physics package with the improved convection and prognostic cloud water/ice and snow/rain waters without supercooled water appears to be adequate for the RSM having an effective horizontal grid size of 50 km or smaller.

Acknowledgments

The authors gratefully appreciate the substantive and thought-provoking comments from Jack Kain and two anonymous reviewers, which significantly improved the manuscript. The authors are also grateful to Joseph Gerrity and Hua-Lu Pan for their generous internal reviews.

REFERENCES

Belair, S., D.-L. Zhang, J. Mailhot, 1994 : Numerical prediction of the 10-11 June 1985 squall line with the Canadian regional finite-element model. *Wea. and Forecasting*, 9, 157-172.

Black, T. L., 1994 : The new NMC mesoscale Eta model : Description and forecast examples. *Wea. and Forecasting*, 9, 265-278.

Dudhia, 1989: Numerical study of convection observed during the winter monsoon experiment using a mesoscale two-dimensional model. *J. Atmos. Sci.*, 46, 3077-3107.

Fowler, L.D., D.A. Randall, and S. A. Rutledge, 1996: Liquid and ice cloud microphysics in the CSU general circulation model. Part I: Model description and simulated microphysical processes. *J. Climate,* 9, 489-529.

Hong S.-Y. and H.-L. Pan, 1998 : Convective trigger function for a mass-flux cumulus parameterization scheme. *Mon. Wea. Rev.*, Accepted.

Juang, H.-M. H. and M. Kanamitsu, 1994 : The NMC nested regional spectral model. *Mon. Wea. Rev.*, 122, 3-26.

Juang, H.-M., S.-Y. Hong, and M. Kanamitsu, 1996 : The NCEP regional spectral model: An update. *Bull. Amer. Meteor. Soc.*, 78, 2125-2143

Kanamitsu, M., 1989: Description of the NMC global data assimilation and forecast system. *Wea. and Forecasting*, 4, 335-342.

_____, and Coauthors, 1991: Recent changes implemented into the global forecast system at NMC. *Wea. and Forecasting*, 6, 425-435.

Kuo, Y.-H., R. Reed, and Y. Liu, 1996: The ERICA IOP 5 Storm. Part III: Mesoscale cyclogenesis and precipitation parameterization. *Mon. Wea. Rev.*, 1409-1434.

Lin, Y.-L., R. D. Farley and H. D. Orville, 1983: Bulk parameterization of the snow field in a cloud model. *J. Appl. Meteor.*, 22, 1065-1092.

Mannoji, N., 1995 : An explicit cloud predicting scheme implemented in the Florida State University global spectral model and its impact. *J. Meteor. Soc. Japan*, 73, 993-1009.

Molinari, J. and M. Dudeck., 1986 : Implicit verses explicit convective heating in numerical weather prediction models. *Mon. Wea. Rev.*, 114, 1822-1831.

Randall, D. A. 1995 : Parameterizing fractional cloudiness produced by cumulus entrainment. *Preprint from workshop on cloud microphysics parameterizations in global atmospheric circulation models*. Kananaskis, Canada, 23-25 May 1995(WMO/TD-No. 713).

Rogers, E., T. L. Black, D. G. Deaven, G. J. DiMego, Q. Zhao, M. Baldwin, N. W. Junker, and Y. Lin, 1996 : Changes to the operational "Early" Eta analysis/forecast system at the National Centers for Environmental Prediction. *Wea. and Forecasting*, 11, 391-413.

Rutledge, S. A. and P. V. Hobbs, 1983 : The mesoscale and microscale structure and organization of clouds and precipitation in midlatitude cyclones. Part VIII: A model for the "seeder-feeder" process in warm-frontal rainbands. *J. Atmos. Sci.*, 40, 1185-1206.

____, and _____, 1984: The mesoscale and microscale structure and organization of clouds and precipitation in midlatitude cyclones. Part XII: A diagnostic modeling study of precipitation development in narrow clod-frontal rainbands. *J. Atmos. Sci.,* 41, 2949-2972.

Sundqvist, H., E. Berge, and J.E. Kristjansson, 1989: Condensation and cloud parameterization studies with a mesoscale numerical weather prediction models. *Mon. Wea. Rev.,* 117, 1641-1657.

Tiedtke, M., 1993: Representation of clouds in large scale models. *Mon. Wea. Rev.*,121, 3040-3061.

Zhao, Q. and F. H. Carr, 1997 : A prognostic cloud scheme for operational NWP models. *Mon. Wea. Rev.*, 125, 1931-1953.

Zhang, D.-L., E.-Y. Hsie and M.W. Moncrieff, 1988 : A comparison of explicit and implicit predictions of convective and stratiform precipitating weather systems with a meso-beta scale numerical model. *Quart. J. Roy. Meteor. Soc.,* 114, 31-60.

_____, K. Gao and D. B. Parsons, 1989 : Numerical simulation of an intense squall line during 10-11 June 1985 PRE-STORM. Part I : Model verification. *Mon. Wea. Rev.,* 117, 960-994.

Figure Lists

Fig. 1. Surface analyses for (a) 1200 UTC 15, (b) 1200 UTC 16, and (c) 1200 UTC 17 May 1995. Areas of precipitation are indicated by shading. Tracks of well-defined low pressure areas are indicated by a chain of arrows ; locations of these centers at 6, 12, and 18 hours preceding map time are indicated by small white crosses in black squares.

Fig. 2. Analyzed 500 hPa geopotential height (m) (solid lines), temperature (K) (dotted lines), and wind vector for (a) 1200 UTC 15, (b) 1200 UTC 16, and (c) 1200 UTC 17 May 1995.

Fig. 3. Visible satellite images for (a) 1045 UTC 16, and (b) 1045 UTC 17 May 1995.

Fig. 4. Analyzed 24-h accumulated rainfall (mm) ending at (a) 1200 UTC 16 and (b) 1200 UTC 17 May 1995.Values are box averages on the 25 km RSM grid from station data.

Fig. 5. Predicted 24-h accumulated rainfall (mm) valid at (a) 1200 UTC 16 (24-h forecast time) and (b) 1200 UTC 17 May 1995 (48-h forecast time) from the CLD1 experiment, (c), and (d) from the CLD2, and (e), and (f) from the CLD3 experiments. Shaded areas and dotted lines denote the subgrid scale(implicit) and grid-resolvable (explicit) rain, respectively.

Fig. 6. Domain-averaged, 6-h accumulated (a) total precipitation, (b) grid-resolvable scale(explicit) rain, (c) subgrid scale (implicit) rain, and (d) percentage of subgrid scale (implicit) rain from CLD1 (thick solid lines), CLD2(dotteded lines), CLD3(thin solid lines), and CLD5(dashed lines). Average is obtained over the heavy precipitation region in Fig. 5.

Fig. 7. Time variation of volume averaged q_{ci} (gkg^{-1}). Average is over all the grid points within the model domain.

Fig. 8. Vertical profiles of the area-time-averaged difference of (a) T(K) and (b) q_v (gkg^{-1}) from the

CLD3 experiment for the CLD1 (thick solid lines), CLD2(dotted lines), and CLD5 (dashed lines) expriments. Profiles are obtained from the data sets during the 48-h forecast over the continental United States with 12 min. interval (every 6 time steps).

Fig. 9. Pressure-latitude crosssections of (a) q_{ci}(gkg^{-1}) (thin lines) and q_{rs}(gkg^{-1}) (thick lines) and (c) vertical p-velocity(Pas^{-1}) from the CLD3 experiment at 1200 UTC 16 May 1995 (24-h forecast time) along the line AB in Fig. 5e, and the corresponding results, (b), and (d) from the NGTQ experiments. Dotted lines in (b) denote the negative values. Shaded in (c) and (d) represent the area that RH is greater than 97 %. Thick dashed-dotted lines in the bottom of each figure means the terrain height.

Fig. 10. As in Fig. 5f but for the DELT experiment.

Fig. 11. The temporal evolution of vertical distribution of q_{ci} (gkg^{-1}) (shaded) and q_{rs}(gkg^{-1}) (sold lines) at the point "A", marked in Fig. 10, from the (a) CLD3 and (b) DELT experiments, and the difference of relative humidity(%) (DELT-CLD3). Scales of q_{ci} in (a) and (b) are shown in the bottom of (a). Contour intervals in (c) are 10 % with zero (thick solid), postive (thin solid) and negative (dotted lines) values.

Fig. 12. Vertical profiles of the area-time-averaged θ_e(dotted lines) and θ_{es}(solid lines). derived from the CLD3(thick lines) and VDCI(thin lines) experiments. Profiles are obtained as in Fig. 8.

Fig. 13. Differences of total(solid line), short wave (dotted), and long wave(dashed) radiative heatings (NORA-CLD3). Profiles are obtained as in Fig. 8.

Fig. 14. Differences of T (K) (NOWL-CLD3). Profiles are obtained as in Fig. 8.

Fig. 15. 250 hPa q_{ci} (gkg^{-1}) at 1200 UTC 16 May 1995 (24-h forecast time) from the (a)

CLD3 and (b) NOHD experiments.

Fig. 16. As in Fig. 5 (e) and (f) but for the NOAD experiment.

Fig. 17. Time variation of volume averaged q_{ci} (gkg^{-1}) from the CLD3 (solid), and NOAD(dotted) experiments. Averaged is over all the grid points within the model domain.

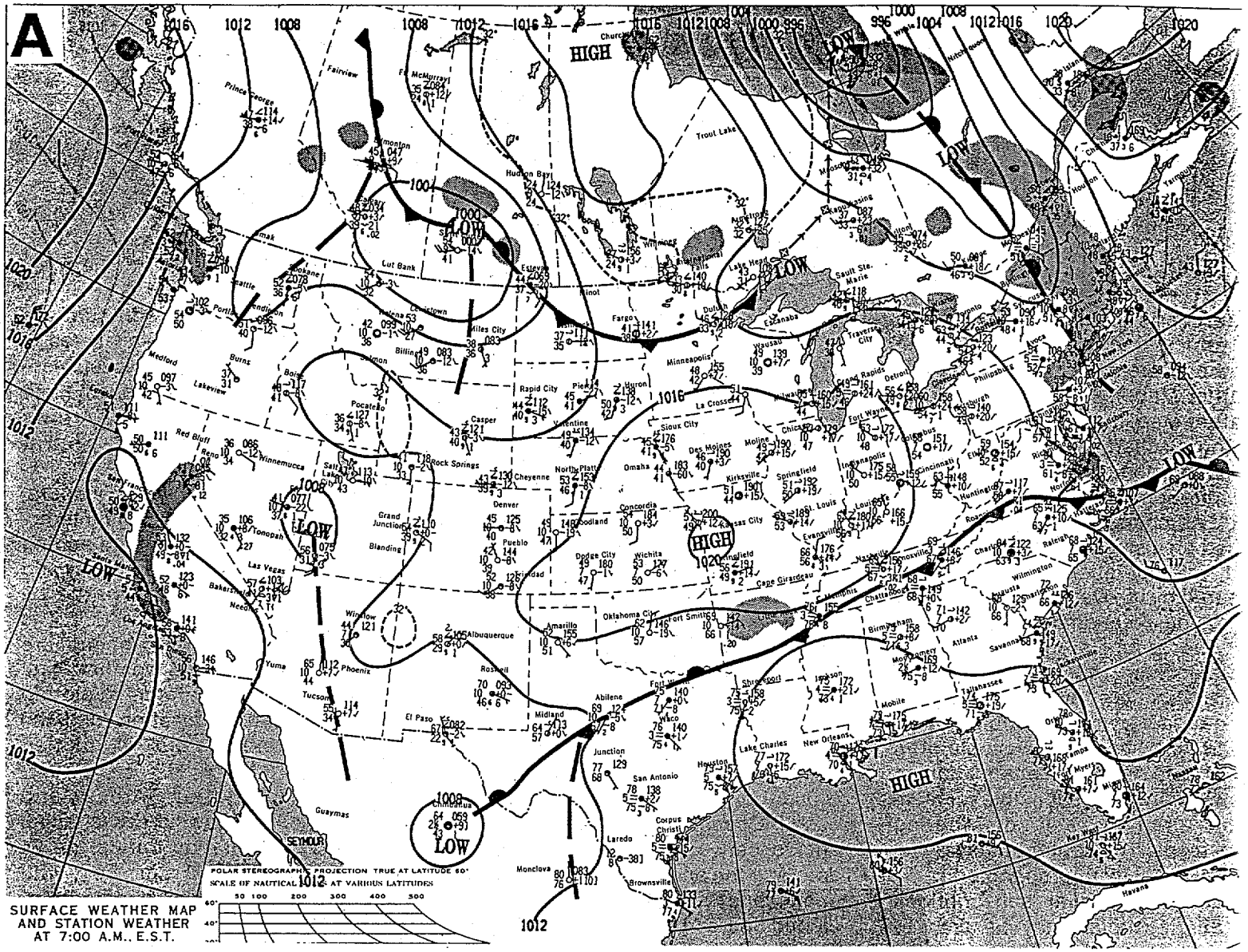

Fig. 1. Surface analyses for (a) 1200 UTC 15, (b) 1200 UTC 16, and (c) 1200 UTC 17 May 1995. Areas of precipitation are indicated by shading. Tracks of well-defined low pressure areas are indicated by a chain of arrows ; locations of these centers at 6, 12, and 18 hours preceding map time are indicated by small white crosses in black squares.

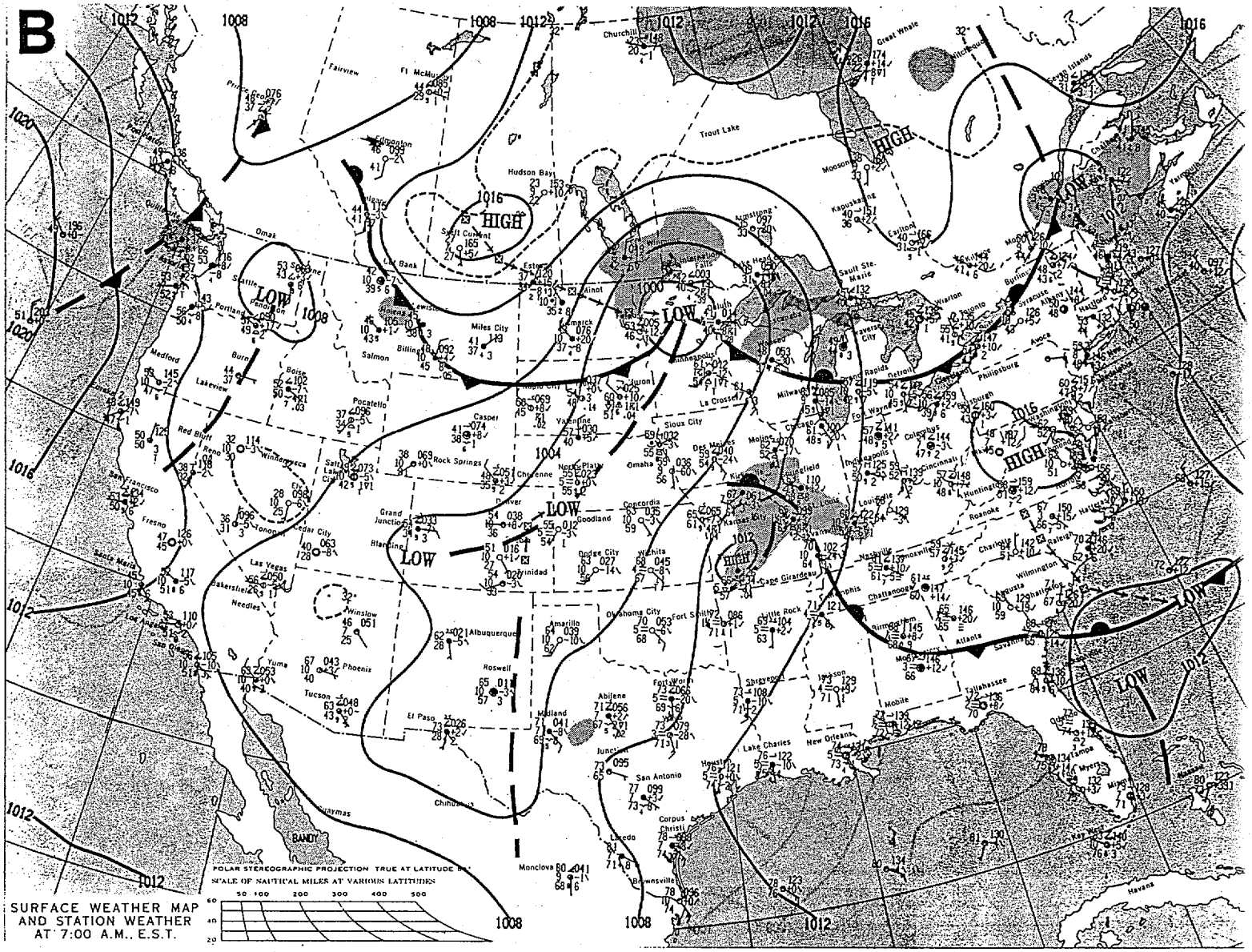

SURFACE WEATHER MAP
AND STATION WEATHER
AT 7:00 A.M., E.S.T.

Fig. 1

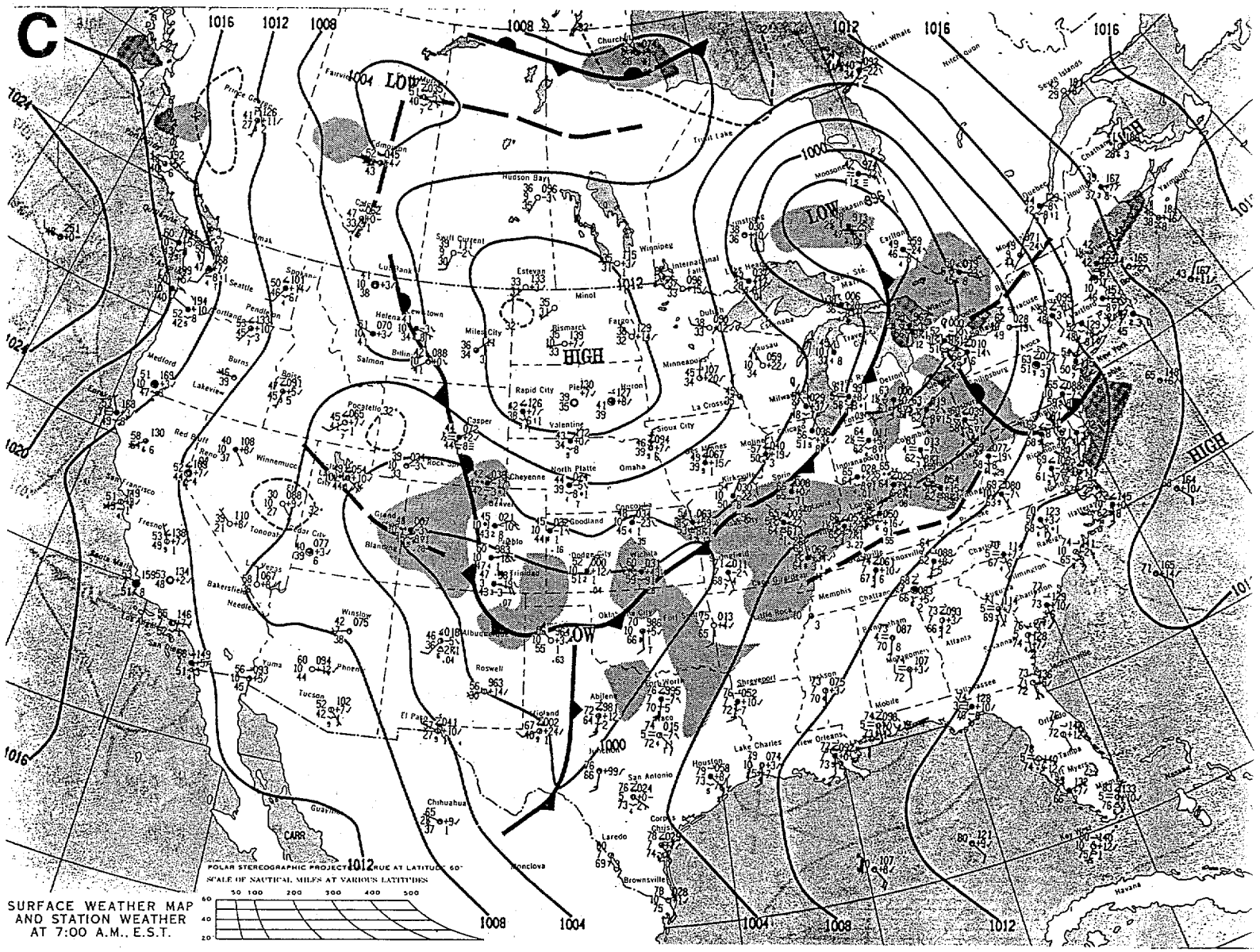

SURFACE WEATHER MAP
AND STATION WEATHER
AT 7:00 A.M., E.S.T.

Fig. 1

(a)500 hPa GPH & T 12Z 15 May 1995

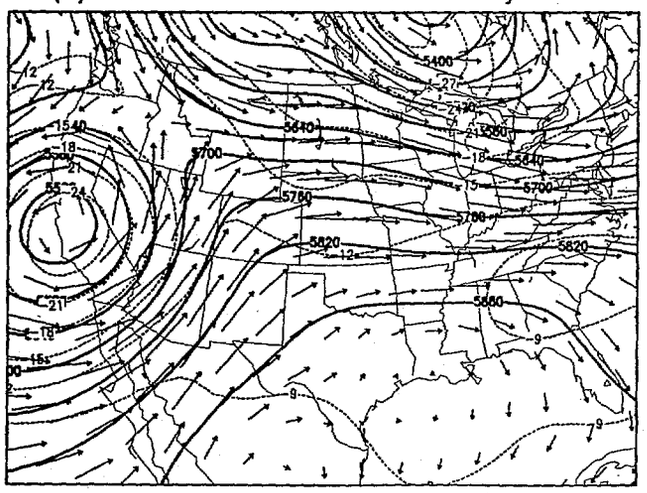

20

(b)500 hPa GPH & T 12Z 16 May 1995

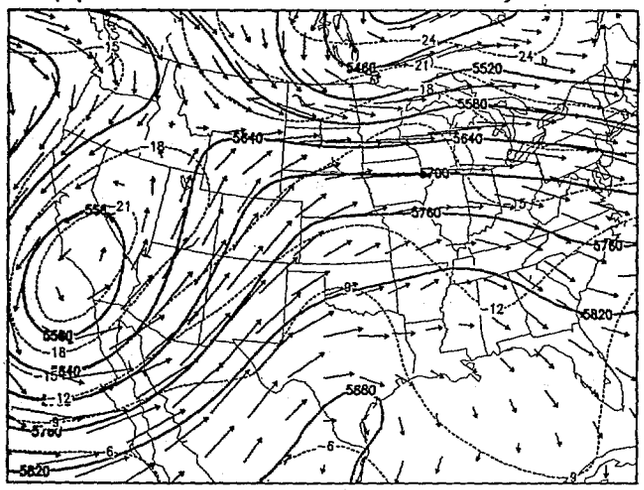

20

(c)500 hPa GPH & T 12Z 17 May 1995

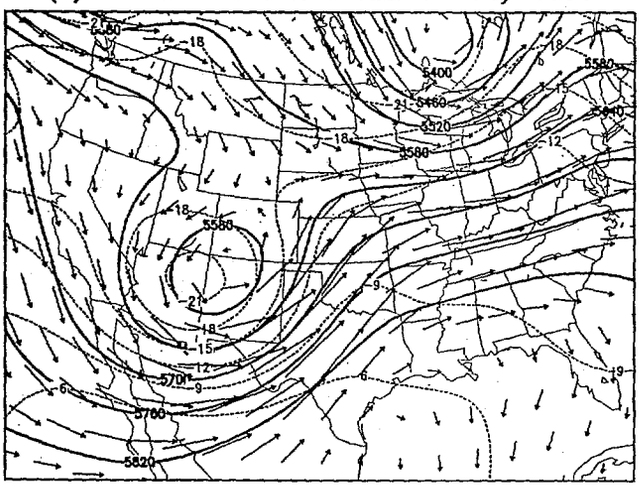

20

Fig. 2. Analyzed 500 hPa geopotential height (m) (solid lines), temperature (K) (dotted lines), and vector for (a) 1200 UTC 15, (b) 1200 UTC 16, and (c) 1200 UTC 17 May 1995.

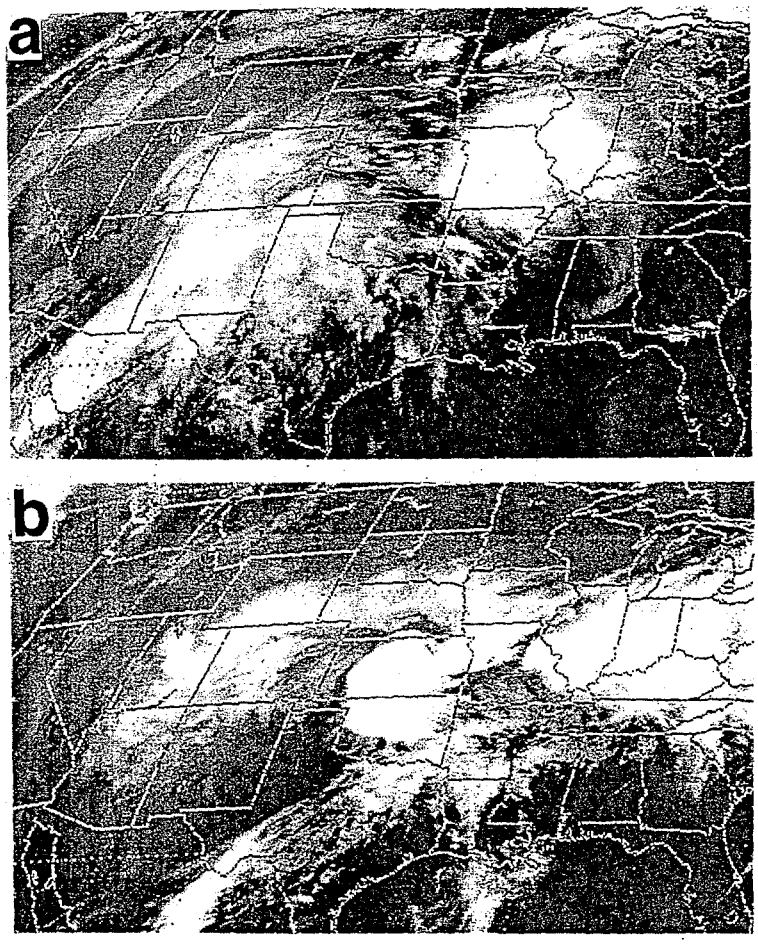

Fig. 3. Visible satellite images for (a) 1045 UTC 16, and (b) 1045 UTC 17 May 1995.

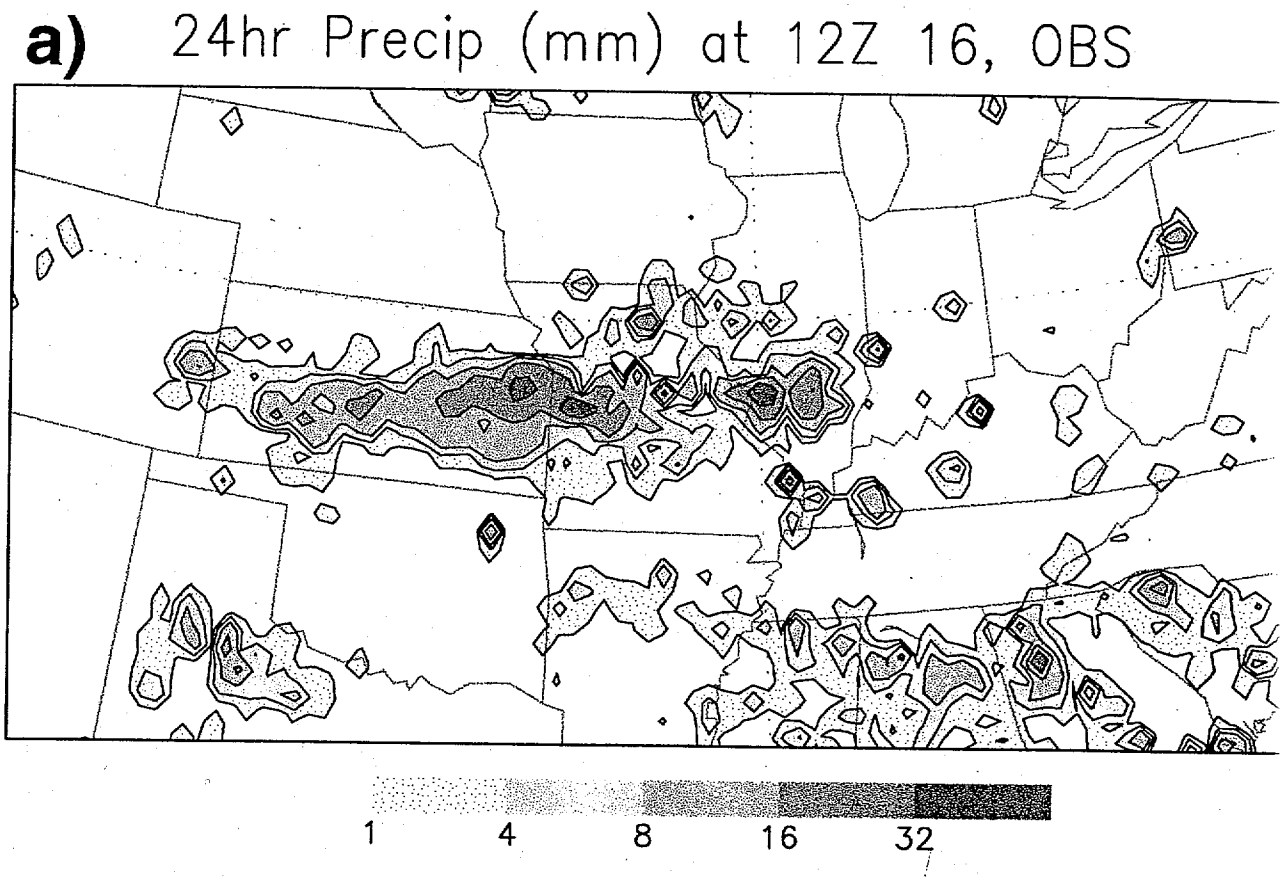

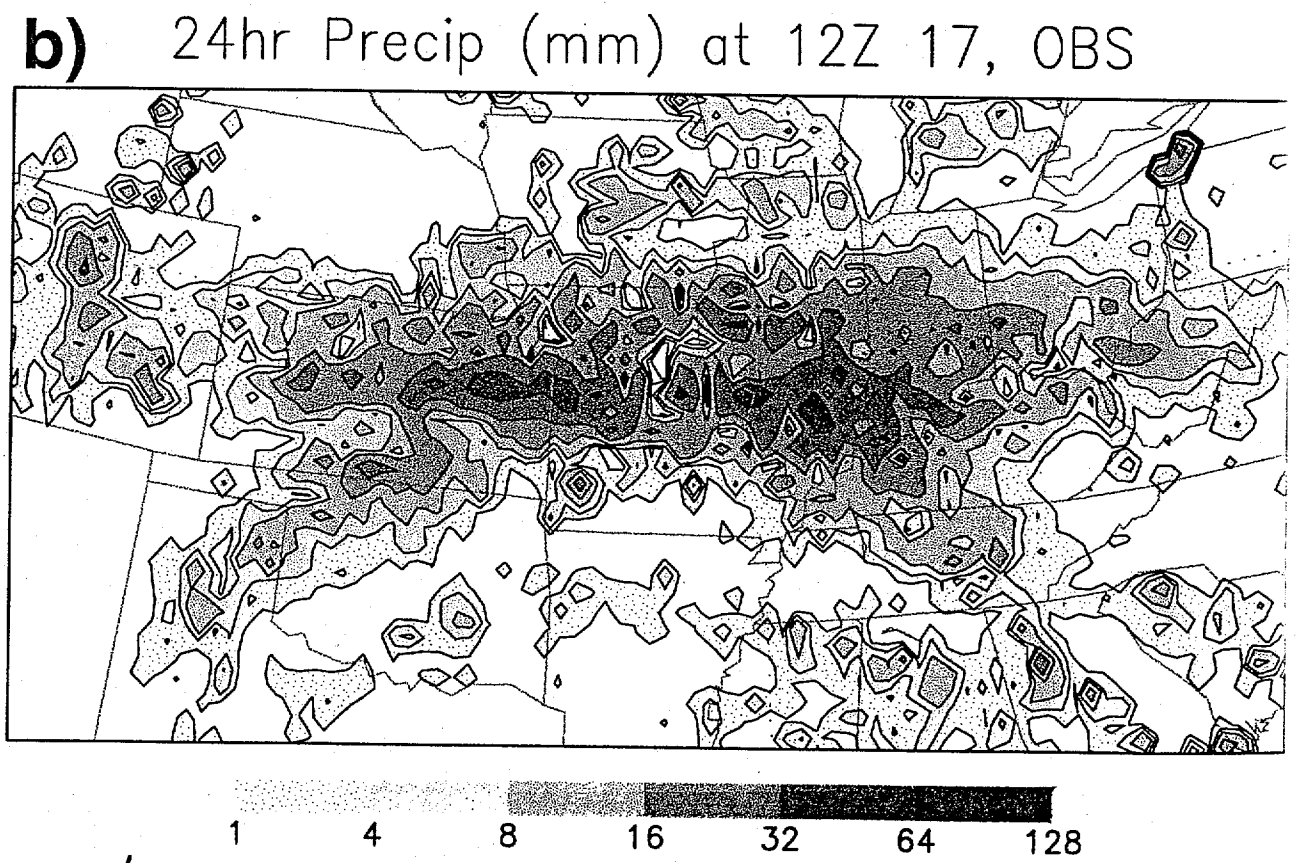

Fig. 4. Analyzed 24-h accumulated rainfall (mm) ending at (a) 1200 UTC 16 and (b) 1200 UTC 17 May 1995. Values are box averages on the 25 km RSM grid from statior

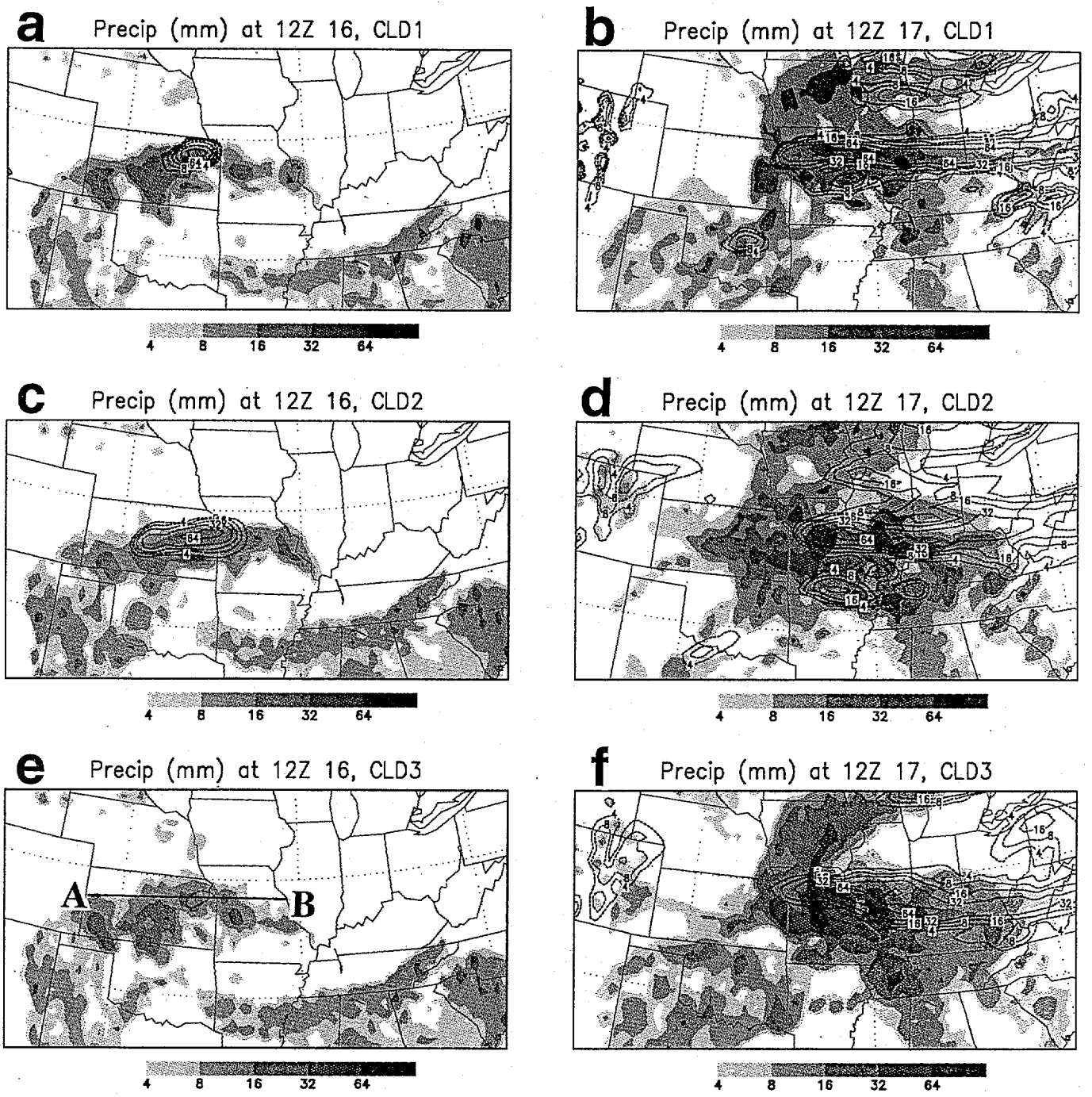

Fig. 5. Predicted 24-h accumulated rainfall (mm) valid at (a) 1200 UTC 16 (24-h forecast time) and (b) 1200 UTC 17 May 1995 (48-h forecast time) from the CLD1 experiment, (c), and (d) from the CLD2, and (e), and (f) from the CLD3 experiments. Shaded areas and dotted lines denote the subgrid scale(implicit) and grid-resolvable (explicit) rain, respectively.

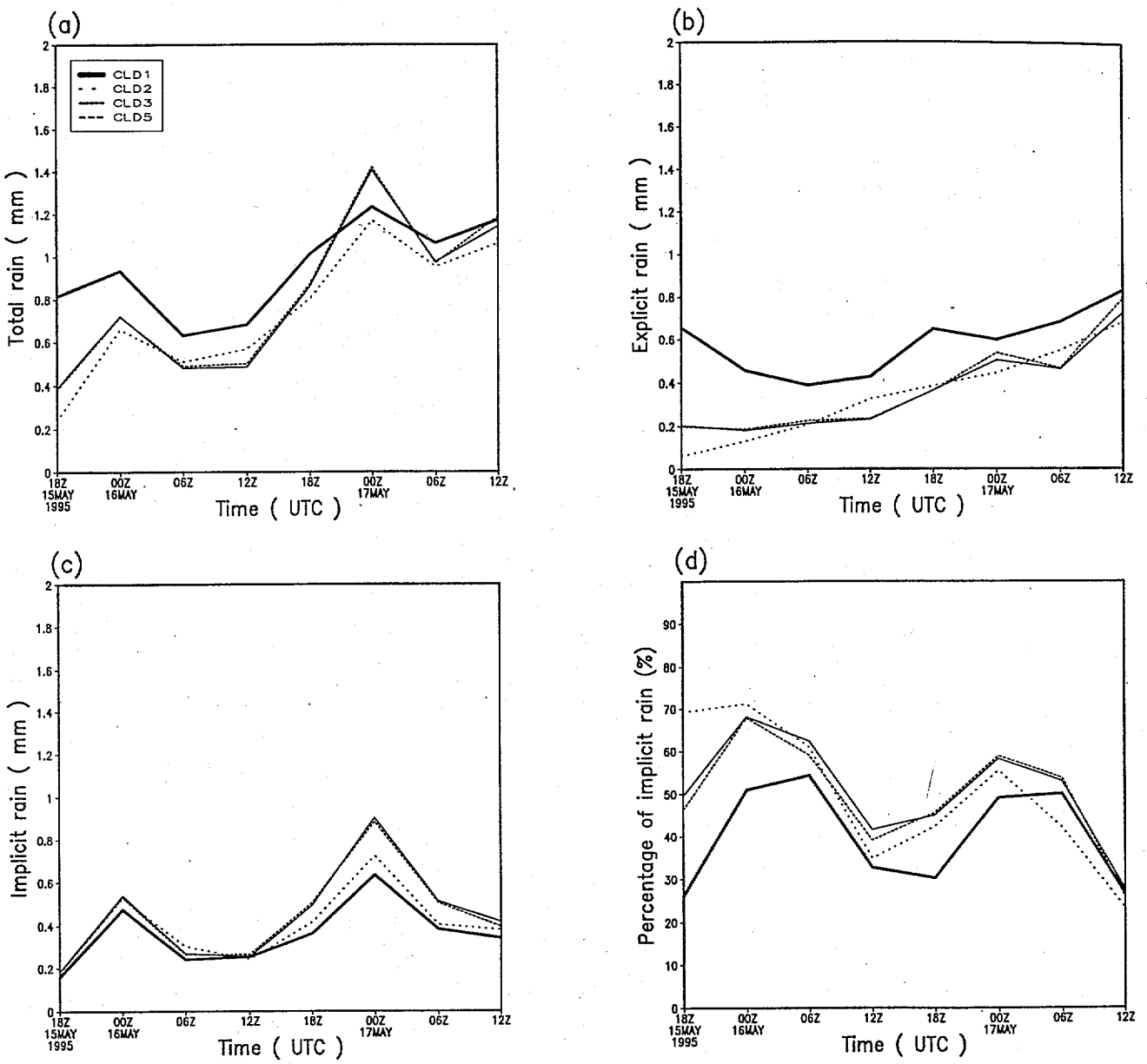

Fig. 6. Domain-averaged, 6-h accumulated (a) total precipitation, (b) grid-resolvable scale(explicit) rain, (c) subgrid scale (implicit) rain, and (d) percentage of subgrid scale (implicit) rain from CLD1 (thick solid lines), CLD2(dotteded lines), CLD3(thin solid lines), and CLD5(dashed lines). Average is obtained over the heavy precipitation region in Fig. 5.

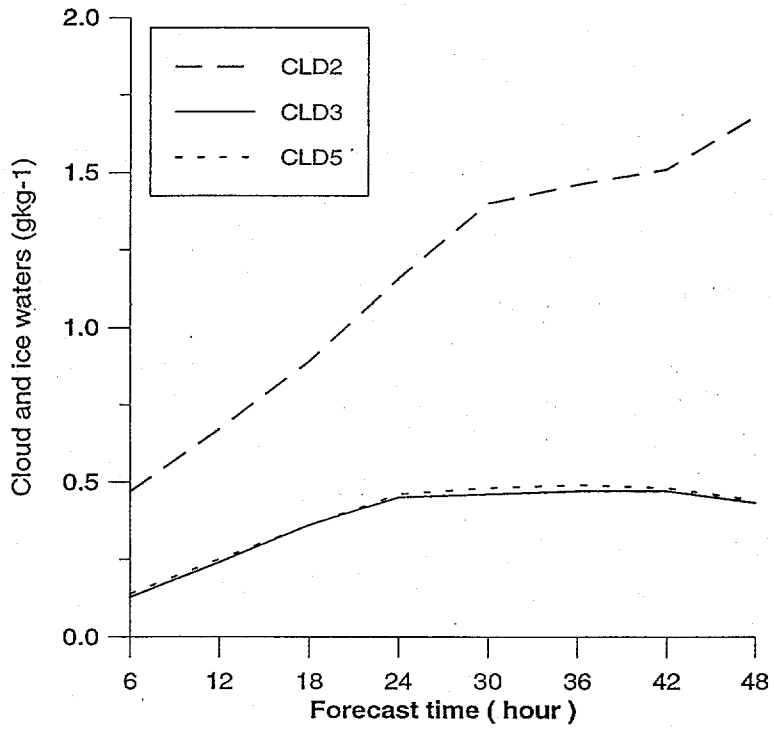

Fig. 7. Time variation of volume averaged q_{ci} (gkg^{-1}). Average is over all the grid points within the model domain.

Fig. 8. Vertical profiles of the area-time-averaged difference of (a) T(K) and (b) q_v (gkg^{-1}) from the CLD3 experiment for the CLD1 (thick solid lines), CLD2(dotted lines), and CLD5 (dashed lines) expriments. Profiles are obtained from the data sets during the 48-h forecast over the continental United States with 12 min. interval (every 6 time steps).

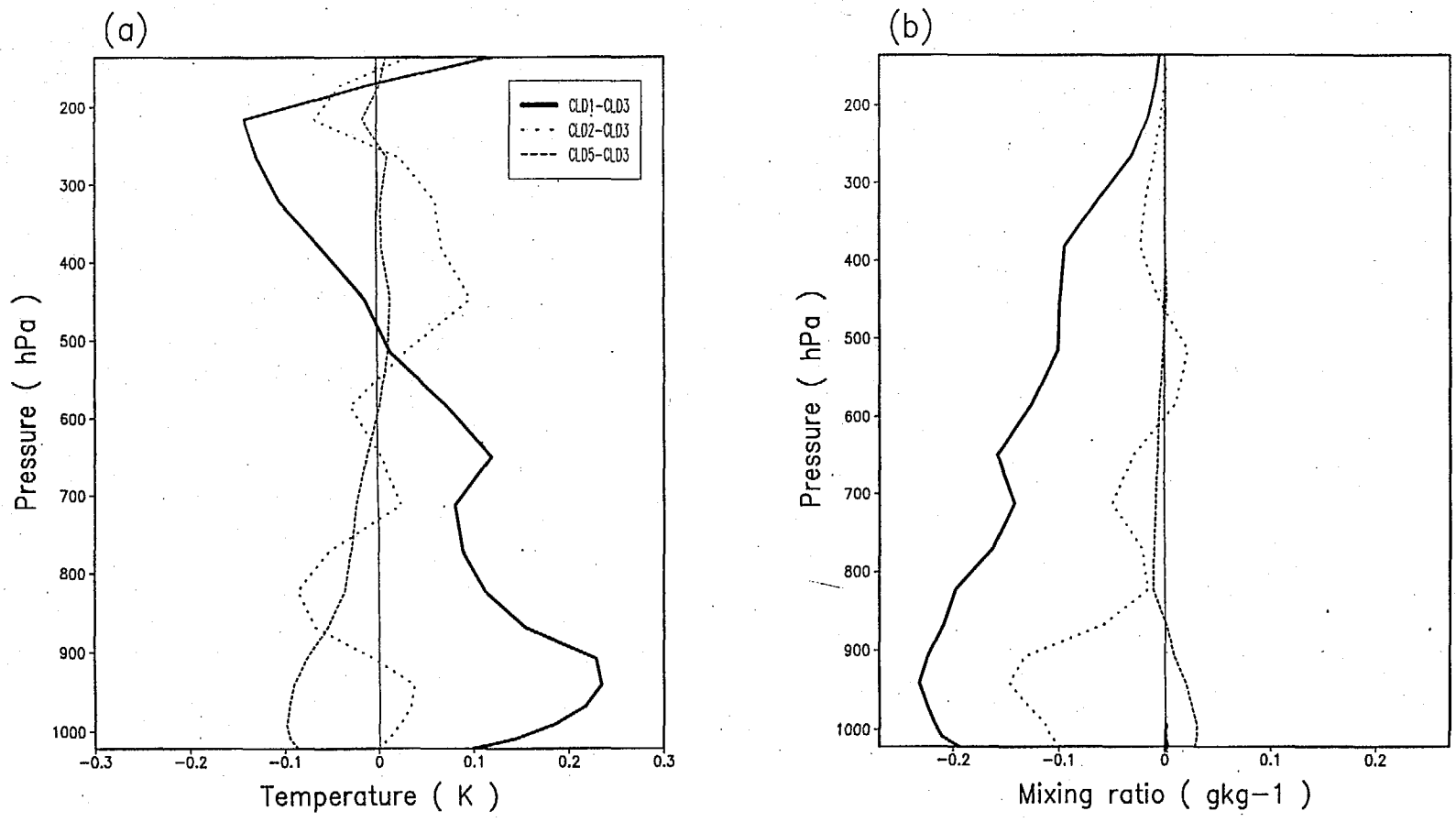

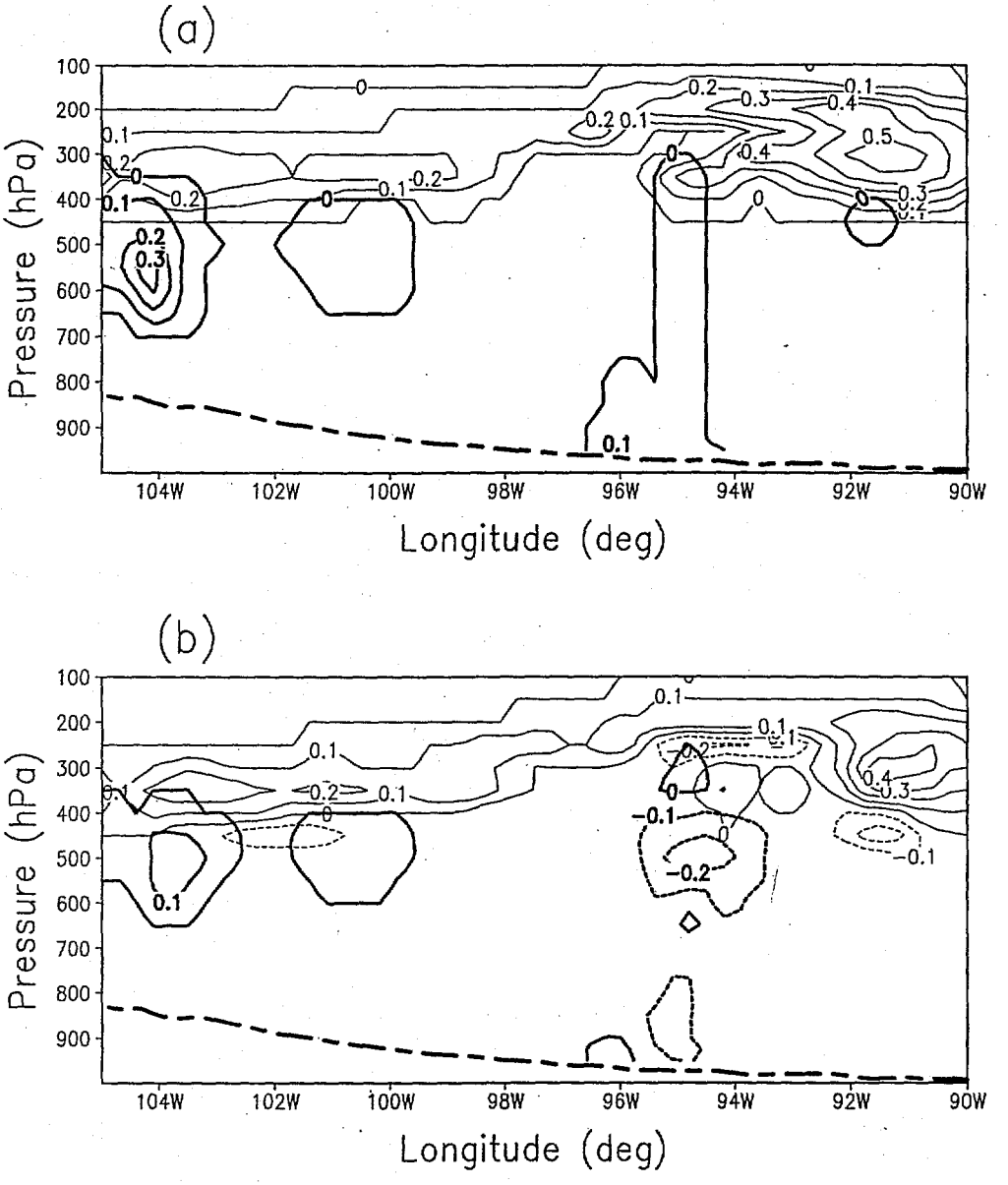

Fig. 9. Pressure-latitude crosssections of (a) q_{ci}(gkg^{-1}) (thin lines) and q_{rs}(gkg^{-1}) (thick lines) and (c) vertical p-velocity(Pas^{-1}) from the CLD3 experiment at 1200 UTC 16 May 1995 (24-h forecast time), along the line AB in Fig. 5e, and the corresponding results, (b), and (d) from the NGTQ experiments. Dotted lines in (b) denote the negative values. Shaded in (c) and (d) represent the area that RH is greater than 97 %. Thick dashed-dotted lines in the bottom of each figure means the terrain height.

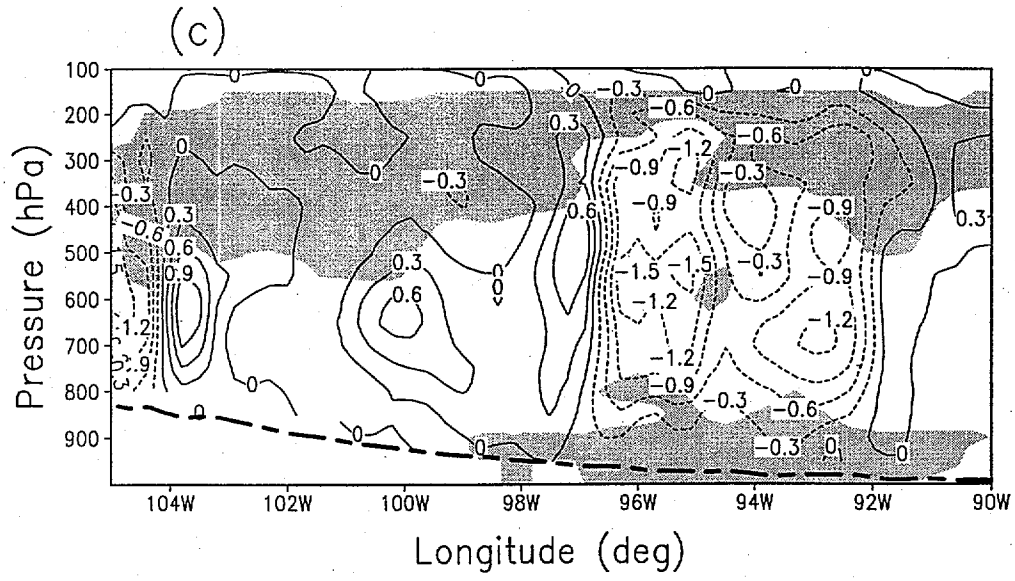
(c)
Pressure (hPa)
100
200
300
400
500
600
700
800
900
104W
102W
100W
98W
96W
94W
92W
90W
Longitude (deg)

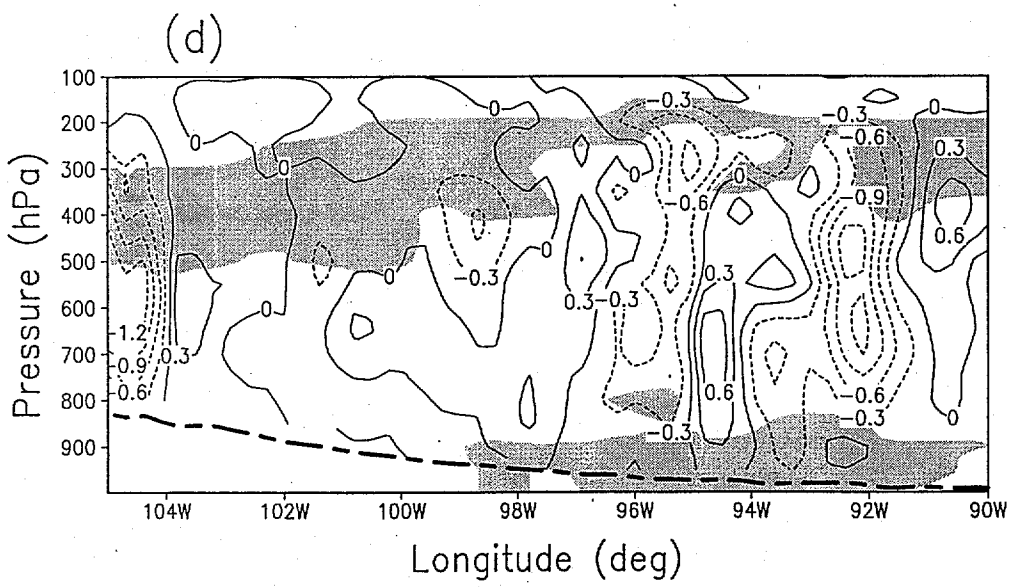
(d)
Pressure (hPa)
100
200
300
400
500
600
700
800
900
104W
102W
100W
98W
96W
94W
92W
90W
Longitude (deg)

Fig 9

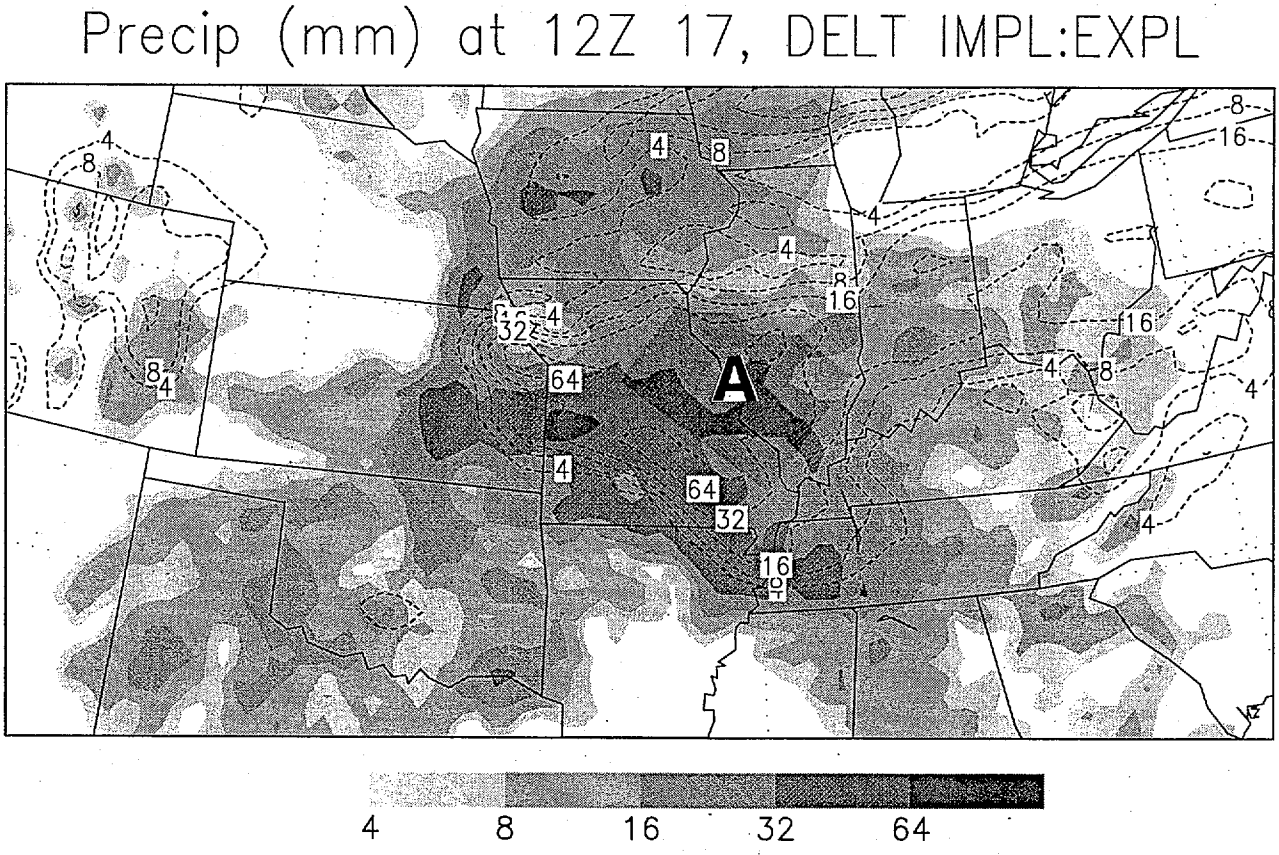

Fig. 10. As in Fig. 5f but for the DELT experiment.

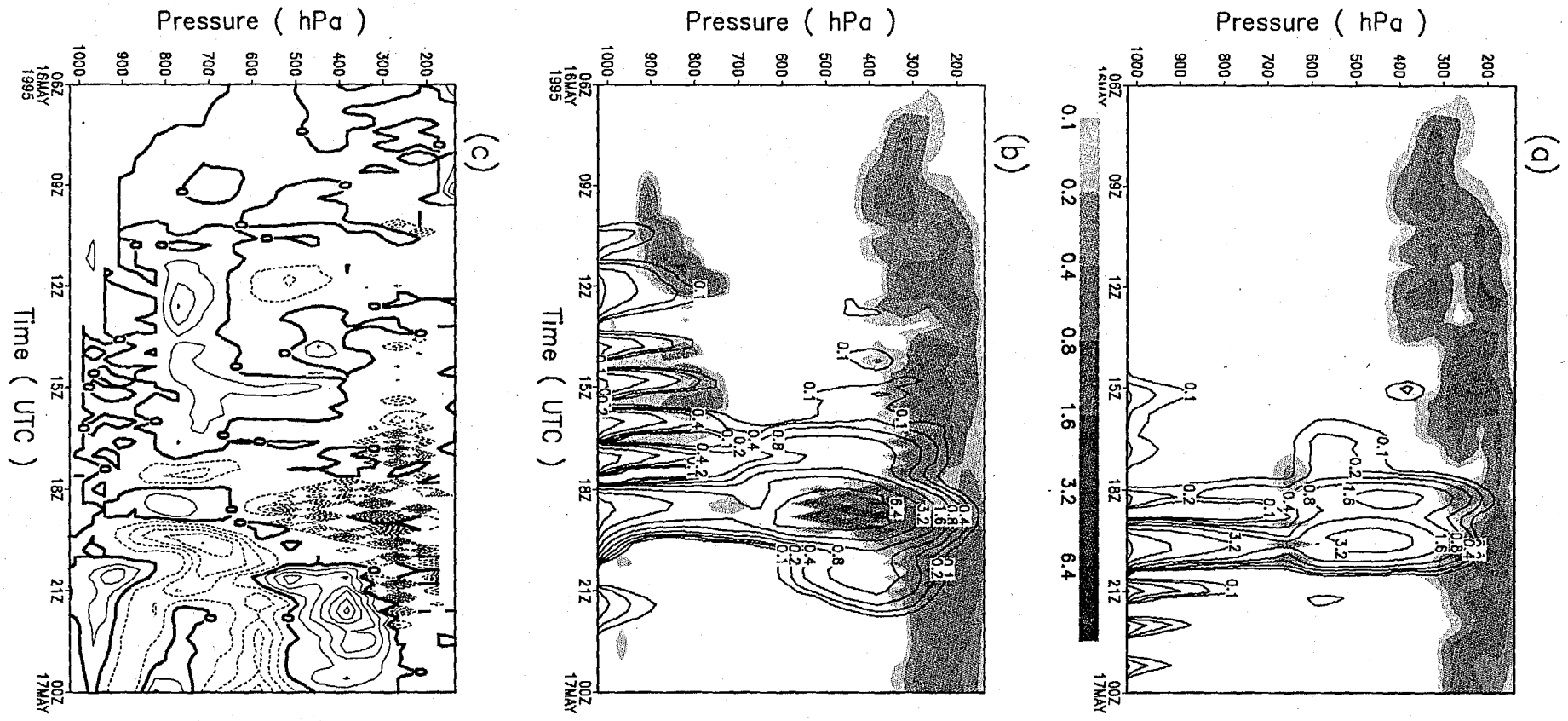

Fig. 11. The temporal evolution of vertical distribution of q_{ci} (gkg^{-1}) (shaded) and q_{rs}(gkg^{-1}) (sold lines) at the point "A", marked in Fig. 10, from the (a) CLD3 and (b) DELT experiments, and the difference of relative humidity(%) (DELT-CLD3). Scales of q_{ci} in (a) and (b) are shown in the bottom of (a). Contour intervals in (c) are 10 % with zero (thick solid), postive (thin solid) and negative (dotted lines) values.

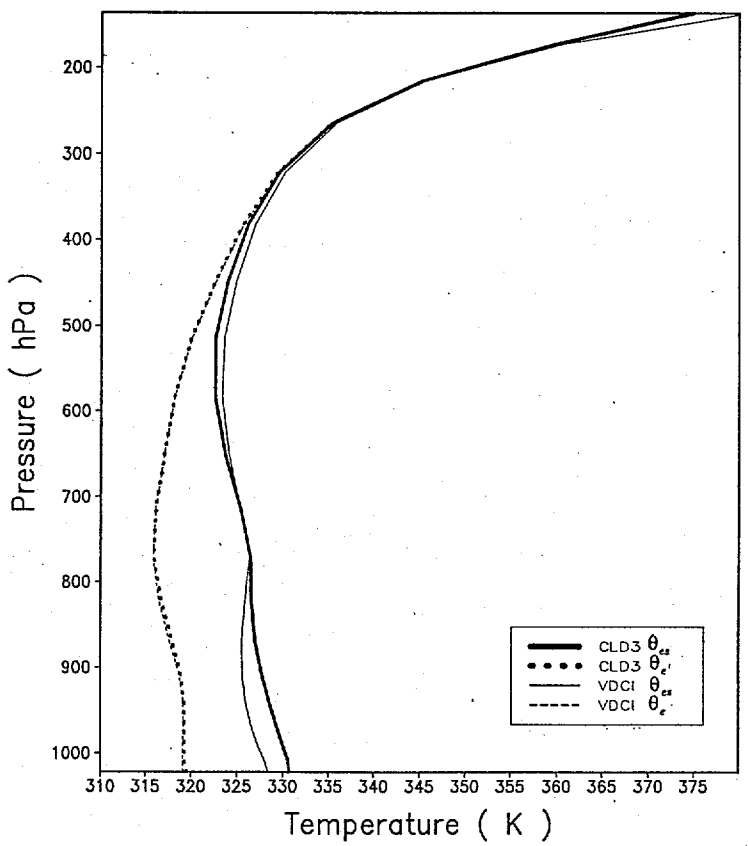

Fig. 12. Vertical profiles of the area-time-averaged θ_e (dotted lines) and θ_{es} (solid lines). derived from the CLD3(thick lines) and VDCI(thin lines) experiments. Profiles are obtained as in Fig. 8.

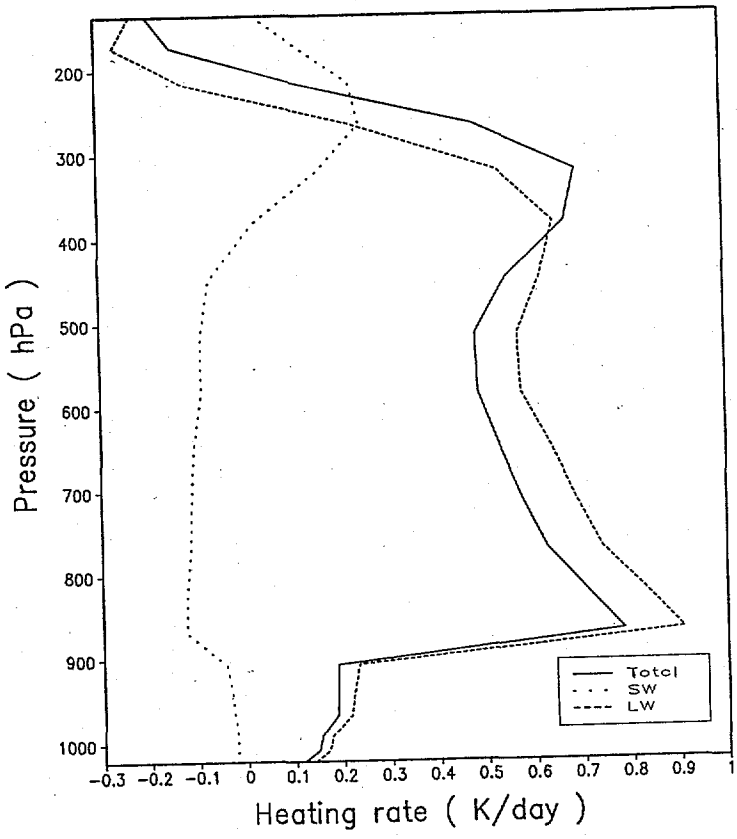

Fig. 13. Differences of total(solid line), short wave (dotted), and long wave(dashed) radiative heatings (NORA-CLD3). Profiles are obtained as in Fig. 8.

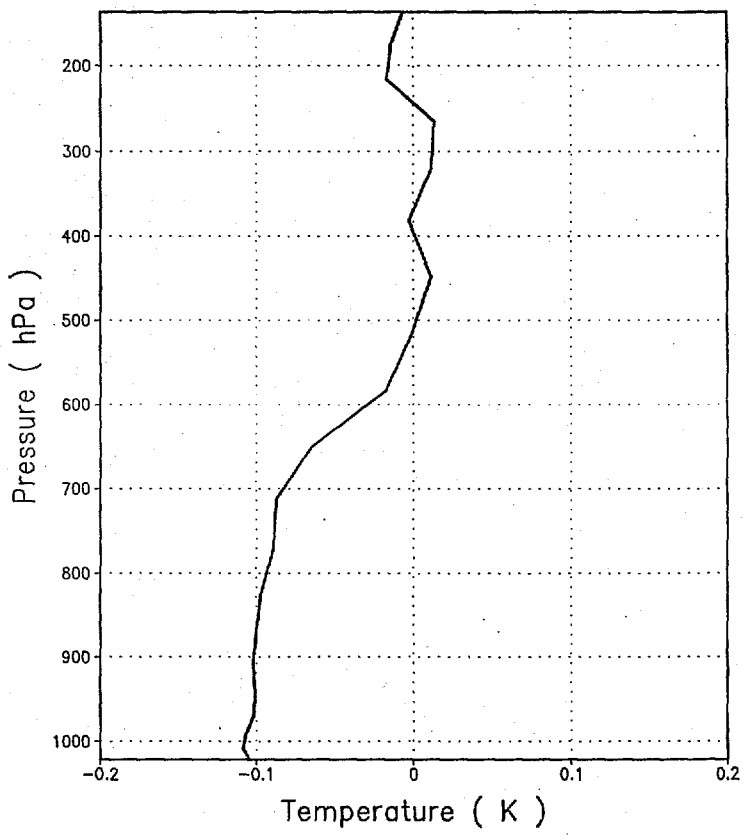

Fig. 14. Differences of T (K) (NOWL-CLD3). Profiles are obtained as in Fig. 8.

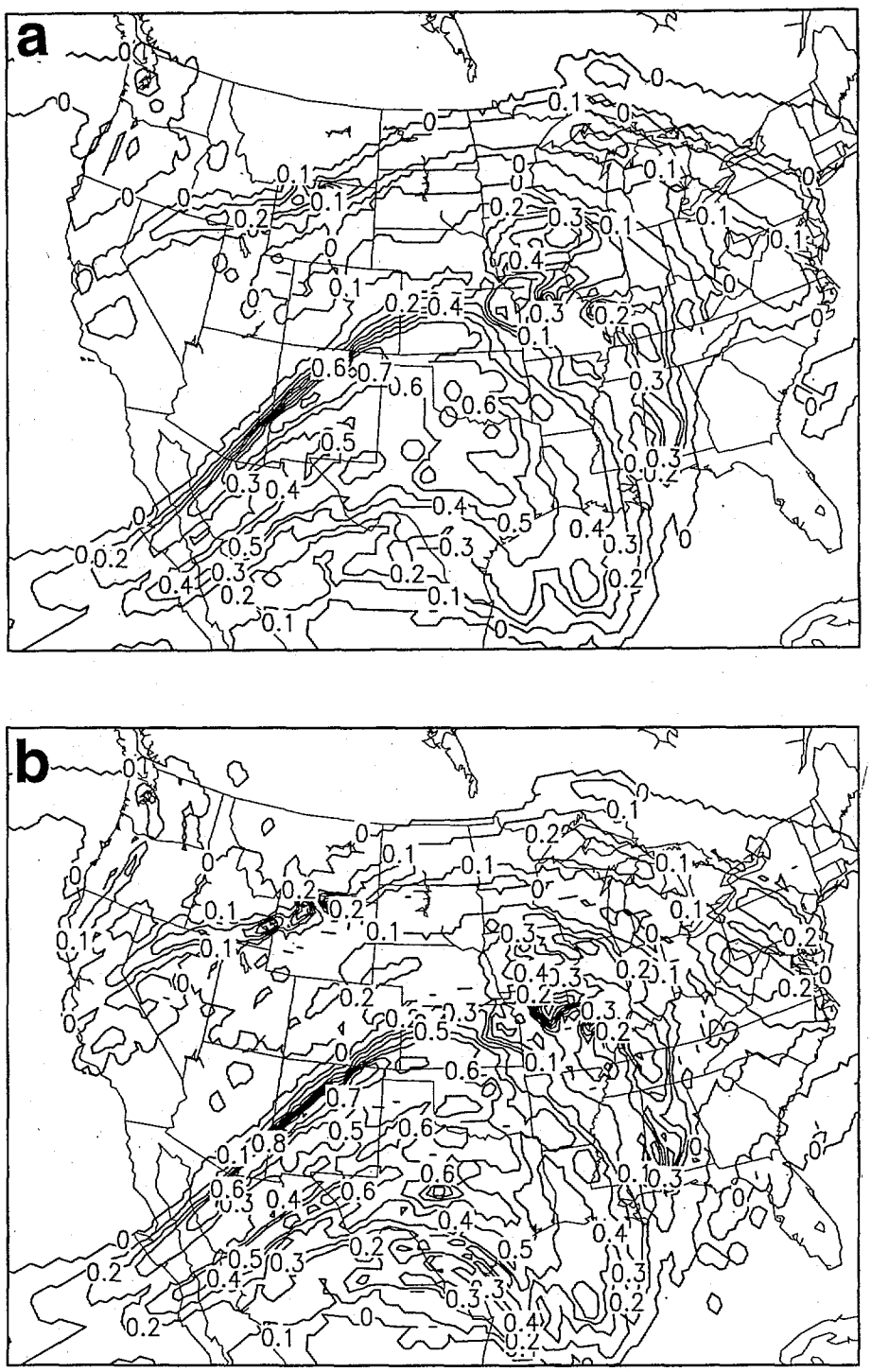

Fig. 15. 250 hPa q_{ci} (gkg^{-1}) at 1200 UTC 16 May 1995 (24-h forecast time) from the (a) CLD3 and (b) NOHD experiments.

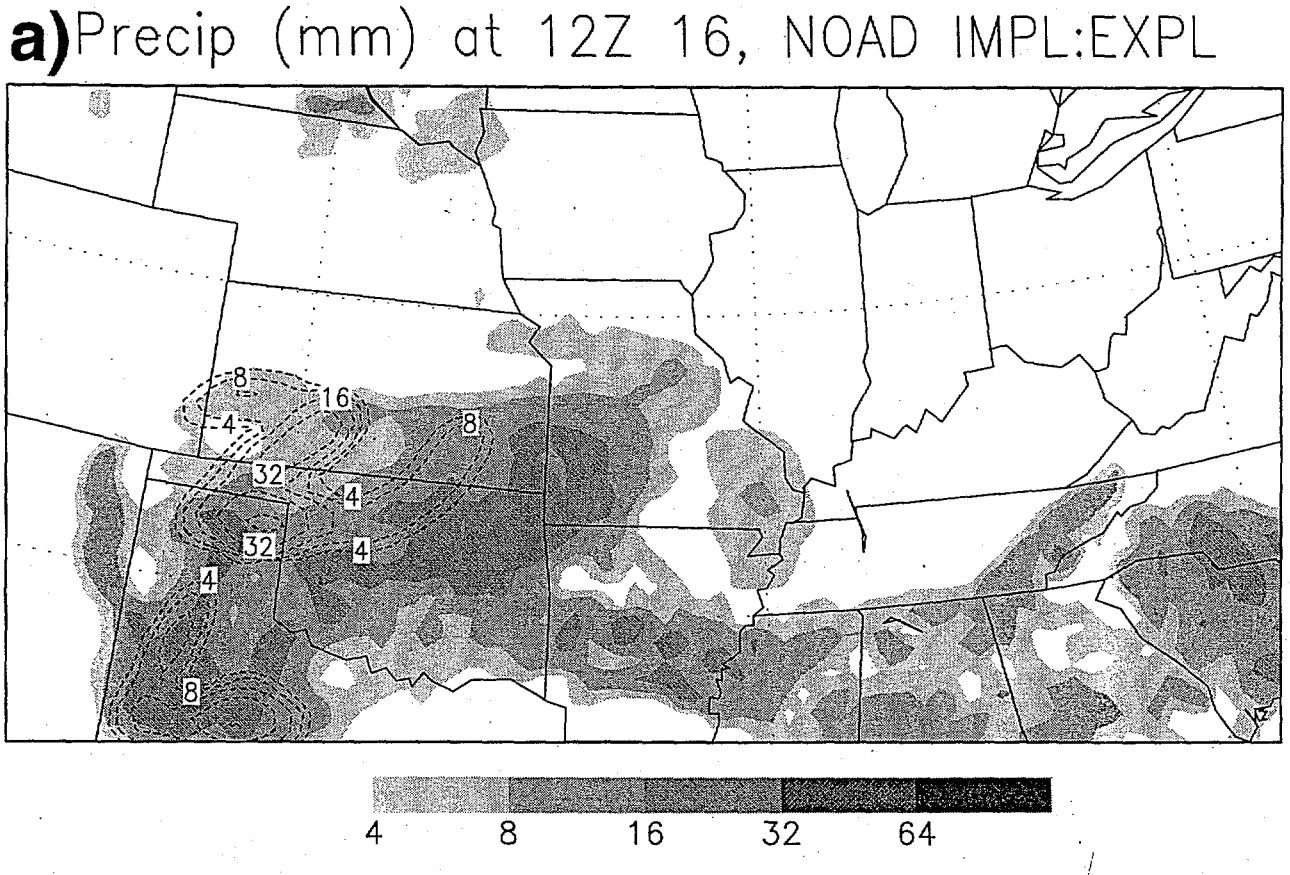

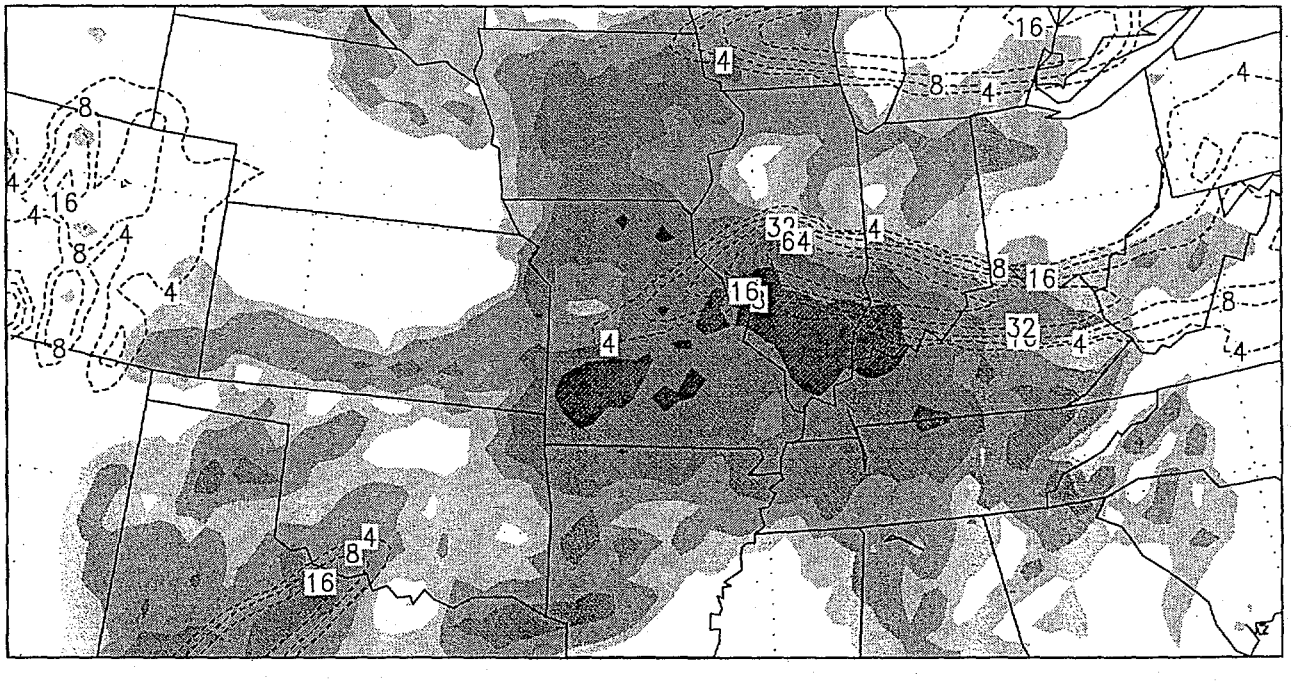

Fig. 16. As in Fig. 5 (e) and (f) but for the NOAD experiment.

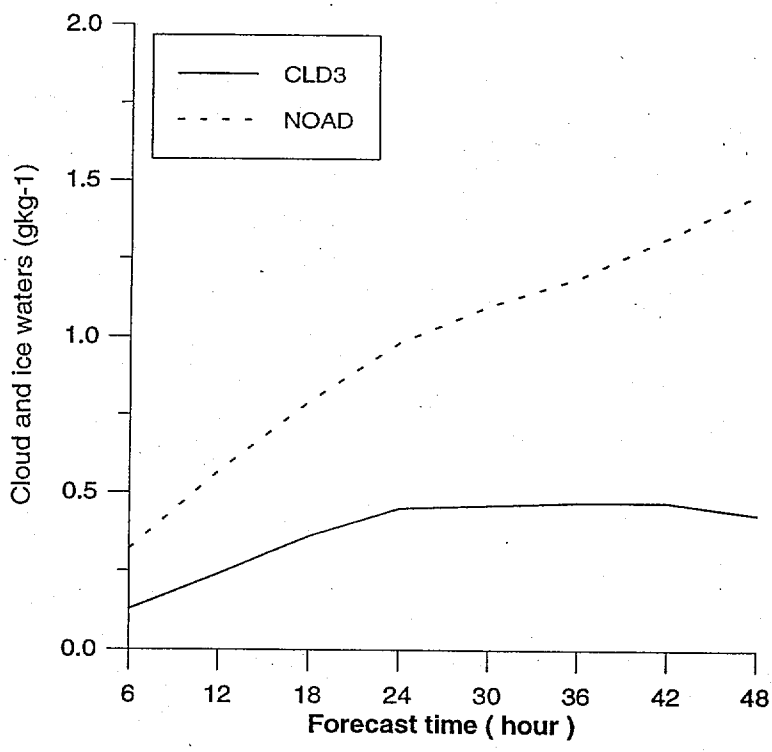

Fig. 17. Time variation of volume averaged q_{ci} (gkg^{-1}) from the CLD3 (solid), and NOAD(dotted) experiments. Averaged is over all the grid points within the model domain.

Appendix A : Cloud microphysics (NCLD=3,NCLD=5)

The microphysics treatment of the source and sink terms are based on Lin et al.(1983), Rutledge and Hobbs(1983) for NCLD=5, and Dudhia(1989) for NCLD=3. NCLD=5 employs five prognostic species including water vapor(q), cloud water(qc), cloud ice(qi), snow(qs), and rain(qr) and NCLD=3 intoduces three prognostic species including water vapor(q), cloud water/ice(qci), and rain/snow(qrs). The reader is referred to original papers for the detailed physical explanations. Subscript R stands for rain and S for snow drops , respectively. Equtation will be given for only rain when its formula for both are identical except for the parameter related to water phase. The definitions of precipitate size and fall velocity are described in section a and , respectively. The source and sink terms for NCLD=5 are described in section c, and the differences between NCLD3 and NCLD5 are pointed out section d. Source terms for the water continuity variables are described in section e. Definitions of variables and constants used below are given in appendix B.

a. Precipitate size distributions

The rain and snow particles are assumed to follow the size distribution derived by Marshall and Palmer(1948), and Gunn and Marshall(1958), respectively. The size distributions for both rain and snow are formulated according to an inverse exponential distribution and its formula for rain can be expressed by

$$N_R(D_R) = N_{0R}\exp(-\lambda_R D_R) \quad , \tag{A1}$$

for rain, where N_{0R} is the intercept parameter of the rain distributions. The slope parameter of the size distributions for rain (λ_R) is determined by multiplying (A1) by drop mass (A4) and integrating over all diameters and equating the resulting quantities to the appropriate water contents ($=\rho q_R$). This may be written as,

$$\lambda_R = \left(\frac{\pi\rho_w N_{0R}}{\rho q_R}\right)^{1/4} . \tag{A2}$$

b. Mass-weighted fall speeds

All particles in the precipitating fields of rain and snow are assumed to fall at their mass-weighted fall speeds, and defined as

$$\overline{V_R} = \frac{\int_0^\infty N_{DR}(D_R)M(D_R)V_R(D_R)dD_R}{\int_0^\infty N_{DR}(D_R)M(D_R)dD_R} \quad . \tag{A3}$$

where the mass distribution is assumed as

$$M(D_R) = \frac{4}{3}\pi\rho_R\left(\frac{D_R}{2}\right)^3 = \frac{\pi\rho_R D_R^3}{6} \quad . \tag{A4}$$

The terminal falling velocity distribution of rain is suggested by Liu and Orville(1969) and given by

$$V_R(D_R) = a_R D_R^{b_R}\left(\frac{\rho_0}{\rho}\right)^{1/2} \quad , \tag{A5}$$

where the density factor in the right hand side of (A5) allows for the change in fall speed with air pressure.

From (A1), (A3) and (A5) , $\overline{V_R}$ may be written as

$$\overline{V_R} = a_R \frac{\Gamma(4+b_R)}{6}\lambda_R^{-b_R}\left(\frac{\rho_0}{\rho}\right)^{1/2} . \tag{A6}$$

c. Sources and sinks of the water continuity variables

1) Condensation and evaporation of water vapor (Pcon)

When water vapor is supersaturated with respect to water, the condensation is determined as,

$$Pcon = \frac{(q_v - q_{sw})/\Delta t}{1 + L_v^2 q_{sw}/(R_v c_{pm} T^2)} \quad , \tag{A7}$$

where q_v, q_{sw} and T used in this process are updated values by other microphysical processes. In other words, *Pcon* removes the additional supersaturated water vapor after other slower processes are taken into account.

If the air is subsaturated and q_c is greater than $q_{\min}$, evaporation of cloud water is given by

$$Pcon = -\min[-Pcon, q_c / \Delta t] \tag{A8}$$

2) Initiation of cloud ice crystal (Pgen)

When T< 0C and the air is supersaturated with respect to ice, the initiation rate of cloud ice from water vapor is given by

$$Pgen = \min[(M_{I0} n_I - q_I) / \Delta t, (q_v - q_{SI}) / \Delta t] \quad , \tag{A9}$$

where it is always, $Pgen \geq 0$. M_{I0} is the initial mass of cloud ice which corresponds to the mass of D_{I0}.

3) Depositional growth of cloud ice (Pisd)

The growth rate by vapor deposition of a small ice crystal is given by

$$\frac{dM}{dt} = \frac{C\,(S_I - 1) / \varepsilon_0}{A_I + B_I} \quad , \tag{A10}$$

where

$$A_I = \frac{L_s}{K_a T}\left(\frac{L_s M_w}{R^* T} - 1\right)$$
$$B_I = \frac{R^* T}{D_f M_w e_{si}} \quad , \tag{A11}$$

where $C = 4\overline{D}_I \varepsilon_0$. The diffusivity and the thermal conductivity of air are, respectively, expressed by

$$D_f = 8.794 \times 10^{-5} T^{1.81} / p$$
$$K_a = 1.414 \times 10^3 \mu \quad , \tag{A12}$$

where dynamic viscosity of air is given by

$$\mu = 1496\times10^{-6}T^{1.5}/(T+120) \quad . \tag{A13}$$

Using (A17), the growth rate of cloud ice via deposition is

$$Pisd = \frac{4\overline{D}_I(S_I-1)n_I}{\rho(A_I+B_I)} = \frac{4D_{Icon}(S_I-1)(q_I n_I)^{1/2}}{\rho L_s^2/(K_a R_v T^2)+1/(q_{sw}D_f)} \quad . \tag{A14}$$

4) Autoconversion of cloud water (ice) to rain (snow) (Paut)

Autoconversion is the process whereby cloud water(ice crystals) droplets form raindrops (snow) through collisions with each other. Following Kessler(1969), the autoconversion rate of cloud water to rain may be written as

$$Paut_C = \alpha(q_C - q_{C0}) \quad , \tag{A15}$$

where α is a rate coefficient and q_{C0} the mass threshold value for autoconversion.

For cloud ice, the conversion rate is given by

$$Paut_I = \max[(q_{Ii} - M_{Imax}n_I)/\Delta t, 0] \quad , \tag{A16}$$

where M_{Imax} represents the maximum allowed ice crystal mass which corresponds to the mass of a D_{IMAX}.

We assume hexagonal plate-like cloud ice crystals. The diameter D_I of a hexagonal plate can be computed from the mass M_I of the plate :

$$D_I = 16.3M_I^{1/2} = 16.3\left(\frac{\rho q_I}{n_I}\right)^{1/2} , \tag{A17}$$

where the ice number concentration n_c is given by Fletcher(1962)'s formula and is given by,

$$n_I = 10^{-2}\exp[0.6(T_0 - T)]/\rho \quad . \tag{A18}$$

5) Collection of cloud water (ice) by rain (snow) and cloud water by snow

The collection rate of cloud water by rain is parameterized by using the continuous collection equation, and is given by

$$\frac{dM(D_R)}{dt} = \pi\left(\frac{D_R}{2}\right)^2 V_R(D_R).\,\rho.q_C.E_{RC} = \frac{\pi}{4}\rho D_R^2 V_R(D_R) q_C E_{RC} \quad . \tag{A19}$$

Multiplying (A19) by (A1), using (A5), and integrating over all particle sizes yields

$$Pacr_{RC} = \frac{\pi a_R q_C E_{RC} N_{0R}}{4}\left(\frac{\rho_0}{\rho}\right)^{1/2} \frac{\Gamma(b_R+3)}{\lambda_R^{b_R+3}} \quad . \tag{A20}$$

Collection of cloud ice by snow($Pacr_{SI}$) is parameterized by replacing subscript R by S and q_c by q_I. In addition, collection of cloud water by snow($Pacr_{SC}$)is also given in the same manner in (A18) by replacing subscript R by S.

6) Evaporation (sublimation) of rain (snow) and depositional growth of snow

The evaporation of rainwater is calculated if the air is subsaturated with respect to water and if the air is above water saturation, growth by condensation occurs. The continuous growth equation is given by

$$\frac{dM(D_R)}{dt} = \frac{C_R D_R (S_w - 1) F_R}{A_w + B_w} \quad , \tag{A21}$$

where $C_R = 2\pi$. The thermodynamic constants are given by,

$$A_w = \frac{L_v}{K_a T}\left(\frac{L_v M_w}{R^* T} - 1\right)$$
$$B_w = \frac{R^* T}{D_f M_w e_{sw}} \tag{A22}$$

The ventilation factor is given by

$$F_R = f_{R1} + f_{R2} S_c^{1/3} R_e^{1/2} \quad . \tag{A23}$$

Using (A1) and (A5), the evaporation rate of rain is

$$\mathrm{Prec} = \frac{C_R N_{0R}(S_W - 1)}{\rho(A_W + B_W)} \times \left[\frac{f_{R1}}{\lambda_R^{\ 2}} + f_{R2} S_c^{1/3} \left(\frac{a_R \rho}{\mu} \right)^{1/2} \left(\frac{\rho_0}{\rho} \right)^{1/4} \frac{\Gamma((b_R + 5)/2)}{\lambda_R^{(b_R+5)/2}} \right] \quad . \tag{A24}$$

When the air is supersaturated with respect to water, the condensational growth rate of rain is given by (A24). When the air is subsaturated with respect to ice, the sublimation of snow and the depositional growth rate of snow(Pssd) is given by (A24) with the substitution of subscripts R and w into S and I.

7) Melting (Pmlt) and freezing (Pfrz)

All snow upon melting is assumed to contribute to rain. The snow melted per unit volume is given by

$$\frac{dM}{dt} = \frac{-2\pi}{L_f} K_a D_S (T - T_0) F_S \quad . \tag{A25}$$

Substituting (A23) for snow into (A25), multiplying by (A1) for snow and integrating over all snow sizes, the melting snow can be expressed by

$$Pmlt_S = -\frac{2\pi N_{0S}}{\rho L_f} K_a (T - T_0) \times \left[\frac{f_{S1}}{\lambda_S^{\ 2}} + f_{S2} S_c^{1/3} \left(\frac{a_S \rho}{\mu} \right)^{1/2} \left(\frac{\rho_0}{\rho} \right)^{1/4} \frac{\Gamma((b_S + 5)/2)}{\lambda_S^{(b_S+5)/2}} \right] \quad . \tag{A26}$$

When $T > T_0$, instantaneous melting of cloud ice is assumed and is given by

$$Pmlt_I = q_I / \Delta t \quad . \tag{A27}$$

When $T < T_{00}$ (= -40 C), homogeneous freezing of cloud water(Pfrz) is assumed by

$$Pfrz = q_C / \Delta t \quad . \tag{A28}$$

8) Evaporation of melting snow (Psev)

This term is identical to (A24) for evaporation of snow except that the evaporation is from a liquid surface :

$$Psev = \frac{C_S N_{0S}(S_W - 1)}{\rho(A_W + B_W)} \times \left[\frac{f_{S1}}{\lambda_S^{\,2}} + f_{S2} S_c^{1/3} \left(\frac{a_S \rho}{\mu} \right)^{1/2} \left(\frac{\rho_0}{\rho} \right)^{1/4} \frac{\Gamma((b_S + 5)/2)}{\lambda_S^{(b_S+5)/2}} \right] \quad . \qquad \text{(A29)}$$

d. No-mixed phase scheme (NCLD=3)

This scheme is identical to NCLD=5 which represents the four prognostic variables, cloud water, cloud ice, rain and snow, separately, except that the mixed phase is not allowed. Therefore, some microphysical processes in NCLD=5 should be neglected or simplified. For example, the collection of cloud water by snow($Pacr_{sc}$) and evaporation of melting snow (Psev) are omitted. Since mixed phase does not exist, melting and freezing processes occur at a level instantaneously, and the discrepancies from NCLD=5 are pointed out below,

1) Melting and freezing

As snow falls through the 0C level, it immediately melts to rain. This process is given by

$$Pmlt_S = -\frac{\rho g \overline{V_f} q_{RS}}{\Delta p} \quad . \qquad \text{(A30)}$$

Advection of ice or snow downwards or of rain or cloud upwards through this level also melts or freeze the particles, where

$$Pfrz \,/\, Pmlt = -\frac{\omega(q_{CI} + q_{RS})}{\Delta p} \quad . \qquad \text{(A31)}$$

In both cases, the 0C isotherm is taken to be at a full model level boundary. Melting occurs at the level immediately below this boundary and freezing above it.

e. Source terms for the water continuity variables

The source terms for the five water continuity variables(NCLD=5) are listed below.

For water vapor q_v:

F_v = -[Pcon + Prec + Pgen + Pisd + Pssd + Psev (T> T_0)]

For cloud water q_C:

$$F_C = [Pcon + Psev - Paut_C - Pacr_{RC} - Pacr_{SC} - Pfrz\ (T > T_{00})] + Pmlt_I(T > T_0)]$$

For cloud ice q_I:

$$F_I = [Pgen + Pisd - Paut_I - Pacr_{SI} + Pfrz\ (T > T_{00})] - Pmlt_I\ (T > T_0)]$$

For rain q_R:

$$F_R = [Prec + Paut_C + Pacr_{RC} + Pacr_{SC}\ (T > T_0) - Pmlt_S\ (T > T_0)]$$

For snow q_S:

$$F_S = [Pssd + Psev\ (T < T_0) + Pmlt_S\ (T > T_0) + Paut_I + Pacr_{SI} + Pacr_{SC}\ (T < T_0)]$$

The source for T is :

$$F_T = L_v/c_{pm}\ [Pcon + Prec + Psev]$$
$$+ L_s/c_{pm}\ [Pgen + Pisd + Pssd]$$
$$+ L_f/c_{pm}\ [Pmlt_S - Pmlt_I + Pacr_{SC}\ (T < T_0)]$$

Appendix B: List of symbols

Symbol	Description	Value	SI units
A_w	Thermodynamic term in Pres for rain		$kg^{-1}ms$
A_I	Thermodynamic term in Pres for snow		$kg^{-1}ms$
a_R	Constant in fallspeed relation for rain	842	$m^{(1-br)}s^{-1}$
a_S	Constant in fallspeed relation for snow	1.139	$m^{(1-bs)}s^{-1}$
B_W	Thermodynamic term in Pres for rain		$kg^{-1}ms$
B_I	Thermodynamic term in Pres for snow		$kg^{-1}ms$
b_R	Fall speed exponent for rain	0.8	
b_S	Fall speed exponent for snow	0.11	
C	Capacitance of ice crystal		F
c_p	Specific heat of air at constant pressure	1005	$Jkg^{-1}K^{-1}$
c_{pm}	Specific heat of moist air at constant pressure		m
D_f	Diffusivity of water vapor in air		m^2s^{-1}
D_I	Diameter of hexagonal plate ice crystal		m
D_{I0}	Initial diameter of cloud ice crystals	12.9×10^{-6}	m
D_{Icon}	Constant in mass and size relation of ice crystals	16.3	$mkg^{-1/2}$
D_R	Raindrop diameter		m
D_S	Snow diameter		m
E_{RC}	Rain/cloud water collection efficiency	1	
E_{SC}	Snow/cloud water collection efficiency	1	
E_{SI}	Snow/cloud ice collection efficiency	0.1	
e_{SI}	Saturation vapor pressure over ice		Nm^{-2}
e_{sw}	Saturation vapor pressure over water		Nm^{-2}
F_R	Ventilation factor for rain		
F_S	Ventilation factor for snow		
f_{1R}	Constant in ventilation factor for rain	0.78	
f_{2R}	Constant in ventilation factor for rain	0.32	
f_{1S}	Constant in ventilation factor for snow	0.65	
f_{2S}	Constant in ventilation factor for snow	0.44	

K_a	Thermal conductivity of air		$Jm^{-1}s^{-1}K^{-1}$
L_f	Latent of fusion of water substance	3.34×10^5	Jkg^{-1}
L_s	Latent of sublimation of water substance		Jkg^{-1}
L_v	Latent of condensation of water substance	5×10^6	Jkg^{-1}
M_I	Average mass of cloud ice crystal		kg
M_{Imax}	Maximum mass of cloud ice crystal	9.4×10^{-10}	kg
M_{i0}	Initial mass of cloud ice crystal	10^{-12}	kg
M_R	Mass of rain per unit volume of air		kgm^{-3}
M_S	Mass of snow per unit volume of air		kgm^{-3}
M_W	Molecular weight of water	18.016	
$M(D_R)$	Mass of raindrop of diameter D_R		
$M(D_S)$	Mass of snowflake of diameter D_S		kg
N_{0R}	Intercept value in raindrop size distribution	8×10^6	m^{-4}
N_{0S}	Intercept value in snowflake size distribution	2×10^7	m^{-4}
n_I	Number concentration of cloud ice crystals		kg^{-1}
n_{I0}	Constant in expression for ice crystal concentration	0.01	m^{-3}
p	Pressure		Nm-2
$Pcon$	Condensation of water vapor		$kgkg^{-1}s^{-1}$
$Pisd$	Deposition/sublimation of cloud ice		$kgkg^{-1}s^{-1}$
$Pssd$	Deposition/sublimation of snow		$kgkg^{-1}s^{-1}$
$Psev$	Evaporation of melting snow		$kgkg^{-1}s^{-1}$
$Pacr_{RC}$	Accretion of cloud water by rain		$kgkg^{-1}s^{-1}$
$Pacr_{SC}$	Accretion of cloud water by snow		$kgkg^{-1}s^{-1}$
$Pacr_{SI}$	Accretion of cloud ice by snow		$kgkg^{-1}s^{-1}$
$Pgen$	Initiation of cloud ice		$kgkg^{-1}s^{-1}$
$Paut_C$	Autoconversion of cloud water		$kgkg^{-1}s^{-1}$
$Paut_I$	Autoconversion of cloud ice		$kgkg^{-1}s^{-1}$
$Prec$	Evaporation/condensation of rain		$kgkg^{-1}s^{-1}$
$Pmlt_s$	Melting of snow		$kgkg^{-1}s^{-1}$
$Pmlt_I$	Melting of cloud ice		$kgkg^{-1}s^{-1}$
q_C	Mixing ratio of cloud water		$kgkg^{-1}$
q_{CI}	Mixing ratio of cloud water and cloud ice in NCLD3		$kgkg^{-1}$

q_I	Mixing ratio of cloud ice		$kgkg^{-1}$
q_R	Mixing ratio of rain		$kgkg^{-1}$
q_{RS}	Mixing ratio of rain and snow in NCLD3		$kgkg^{-1}$
q_S	Mixing ratio of snow		$kgkg^{-1}$
q_{C0}	Mixing ratio threshold for $Paut_c$	0.0007	$kgkg^{-1}$
q_{sI}	Saturation mixing ratio with respect to ice		$kgkg^{-1}$
q_{stw}	Saturation mixing ratio with respect to water		$kgkg^{-1}$
q_v	Mixing ration of water vapor		$kgkg^{-1}$
R_v	Gas constant of water vapor	461	$Jkg^{-1}K^{-1}$
S_c	Schmidt number	ν / D_f	
F_C	Source term for cloud water		$kgkg^{-1}s^{-1}$
F_I	Source term for cloud ice		$kgkg^{-1}s^{-1}$
F_R	Source term for rain		$kgkg^{-1}s^{-1}$
F_S	Source term for snow		$kgkg^{-1}s^{-1}$
F_v	Source term for water vapor		$kgkg^{-1}s^{-1}$
T	Temperature		K
T_0	Reference temperature	273.16	K
T_{00}	Threshold temperature for homogeneous freezing	233.16	K
t	Time		s
$\overline{V_r}$	Mass-weighted fallspeed of rain		ms^{-1}
$V_R\ (D_R)$	Fallspeed of raindrop of diameter D_r		ms^{-1}
$\overline{V_s}$	Mass-weighted fallspeed of snow		ms^{-1}
$V_S\ (D_S)$	Fallspeed of snowflake of diameter D_s		ms^{-1}
x	Horizontal distance		m
z	Vertical distance		m
α	Rate coefficient for autoconversion	0.001	s^{-1}
β	Constant in ice crystal concentration	0.6	K^{-1}
Γ	Gamma function		
ε_0	Permittivity of free space ???		
ρ	Air density		kgm^{-3}
ρ_0	Reference air density	1.28	kgm^{-3}

ρ_w	Density of water	1000	kgm^{-3}
ρ_{sS}	Density of snow	100	kgm^{-3}
λ_R	Slope of raindrop size distribution		m^{-1}
λ_S	Slope of snowflake size distribution		m^{-1}
μ	Dynamic viscosity of air		$kgm^{-1}s^{-1}$
ν	Kinematic viscosity of air		m^2s^{-1}
κ	R_d/C_p	0.2857	